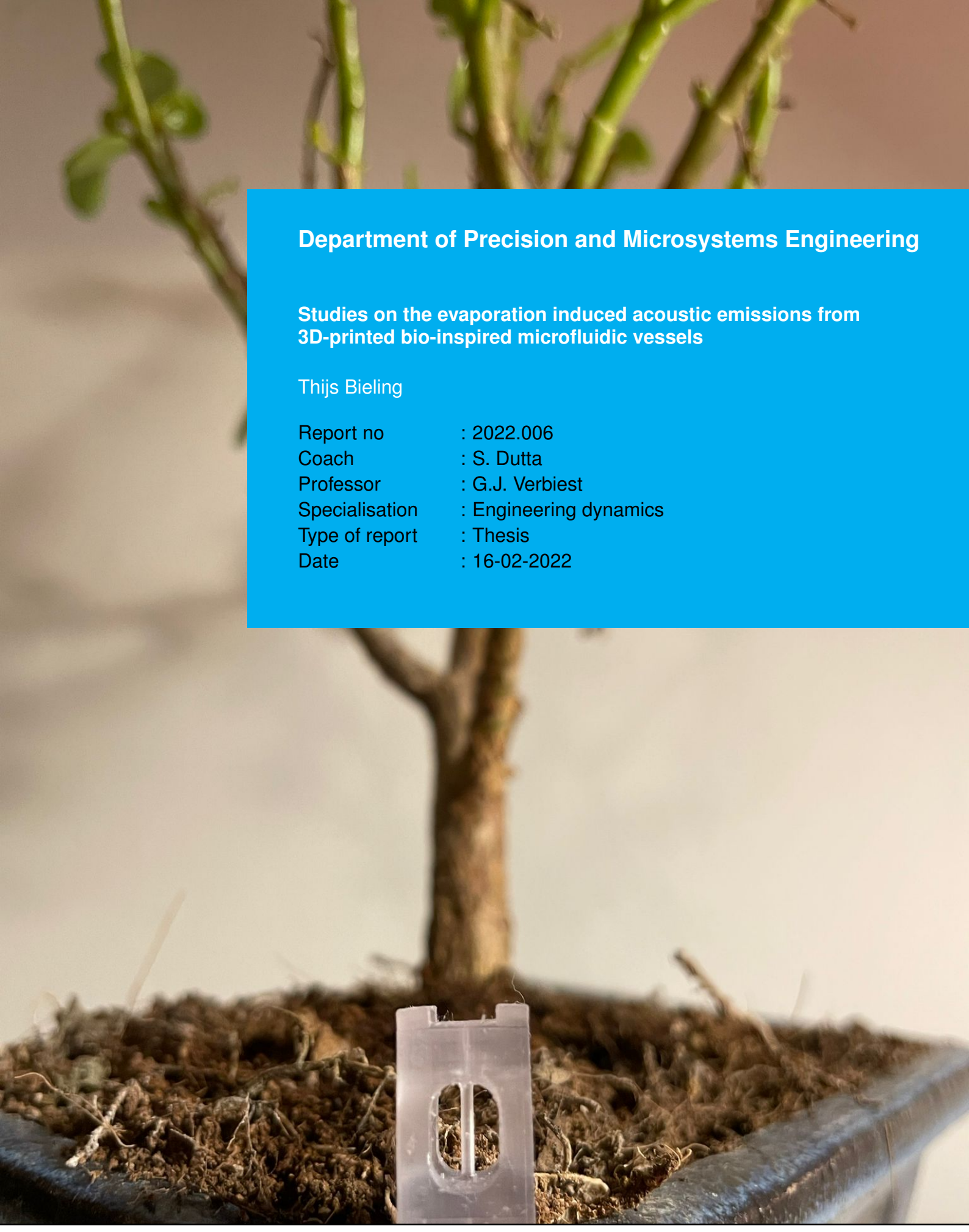

Department of Precision and Microsystems Engineering

Studies on the evaporation induced acoustic emissions from 3D-printed bio-inspired microfluidic vessels

Thijs Bieling

Report no	: 2022.006
Coach	: S. Dutta
Professor	: G.J. Verbiest
Specialisation	: Engineering dynamics
Type of report	: Thesis
Date	: 16-02-2022

TU Delft Delft University of Technology

Challenge the future

Preface

This thesis was written for my Master of Science in Mechanical Engineering at the TU Delft. The topic was chosen within the track of High-Tech Engineering and the focus area of Engineering Dynamics. My supervisors, Dr. Gerard Verbiest and Dr. Satadal Dutta have studied the application of ultrasound in agriculture for the 4TU Plantenna project. Their recent study observed a relation between the geometrical and material properties of xylem vessels in plants and the drought-induced acoustics emissions from plant shoots. We performed the studies presented in this thesis to further study the predicted formulas for these acoustics. This study took the approach of 3D printing artificial plant structures and inducing acoustics on these structures through dehydration. These acoustics were then studied in the time and frequency domain.

Significant findings include revealing three major types of acoustic pulses originating from these vessels and multiple sources of acoustic events. Furthermore, the variation of the vessel geometry of this artificial plant showed how the frequency content of the pulses was seen to shift down with increasing vessel radius while it remained roughly constant for varying vessel lengths. These findings provide new insights into acoustic emissions from microfluidic devices and plants. With the help of this research, we made further advancements on the Plantenna project and worked towards a more robust understanding of acoustic emissions and their attenuation not only in xylem vessels but also in 3D printed microfluidic devices.

As a final note for this preface, I would like to thank my supervisors Gerard and Satadal for their excellent guidance and reachability during the project. I would also like to thank the technicians Patrick van Holst, Bradley But and Gideon Emmaneel for their helping hand and expertise in the lab. Finally, I would like to thank my girlfriend, family, roommates and friends for their emotional support during my year of working on this thesis.

Thijs Bieling
February 16, 2022

Contents

Chapter 1

Introduction

In 1966, Milburn and Johnson [1] detected acoustic emissions in plants induced by drought stress. This experiment sparked interest as it would allow for detecting drought stress in plants in-situ without destroying the plant itself or measuring the plant's environment. Furthermore, watering plants using these emissions becomes possible in a non-destructive manner and before permanent damage occurs. Subsequently, a multitude of experiments was done in order to find a way of relating the origin of these acoustic emissions and their dependency on the quantum of drought stress across a myriad of plant species [2, 3, 4, 5, 6]. Tyree et al. [3] used these events to plot the subsequent loss of hydraulic capacity against the cumulative amount of acoustic events. Above 1 MPa of pressure difference, they found that "cavitations" were induced. That is to say, the tension in the vessel suddenly relaxes by the appearance of an air bubble that subsequently blocks the vessel. More research followed into cumulative acoustic events, lacking regard for the underlying signal interpretation. More recently, researchers have started to look into obtaining more information on the interpretation of the signal recorded from these acoustic events [7, 8, 9, 10].

Despite this research, there is still a lack of studies on the exact origin and signal characteristics of most acoustic emissions from plants, even below the cavitation threshold. One study which did make great strides was done in 2014 by Ponomarenko et al. [11], who combined optical and acoustic measurements on a slab of wood in hydrogel. They showed how two sources of "cavitation" occur in the xylem vessel; those induced by cavitation and those with air bubbles introduced by neighbouring vessels that subsequently nucleated. Furthermore, they also linked each acoustic emission to one vessel cavitating/nucleating. Finally, Ponomarenko showed how the acoustic energy of the pulses correlates to the volume of the vessel it originates from, connecting them to the elastic energy of the vessel.

This observation was utilised by Dutta et al. [12], who related geometrical and viscoelastic xylem vessel properties to time- and frequency-domain characteristics for the recorded acoustic events. These acoustics were then compared to plant features showing relations between the two. Further advancement of these types of studies can prove useful for the early diagnosis of drought stress in plants and non-invasive monitoring of liquid flow in microfluidic devices.

The idea of this thesis is to study the acoustic emissions in a bio-inspired vessel of known geometry, compared to the wide array of xylem vessel radii from which acoustics could originate in plants. Several examples of such bio-inspired xylem vessels exist in the literature. Dixon et al. [13] scanned the parenchyma of bamboo and subsequently scaled up and printed this structure to study the density and Young's modulus. Another artificial structure is the by Wang et al. [14] created synthetic mangrove for desalination purposes. Here they used a silica frit as the xylem vessels and defined the roots and leaves of the plant with hydrogel and an AAO membrane. A third example of a bio-inspired xylem vessel is that by Shi et al. [15] who used a nanoporous ceramic disk to provide suction on 3mm diameter tubes mimicking the flow of water in a tree.

We chose to 3D print our xylem vessels and studied acoustic emissions from these structures in a controlled environment with all known parameters. Using this structure, we hope to further validate the proposed formulae with these acoustics as the predicted values should match the printed values. If the by Dutta et al. [12] proposed formulae are proven correct, acoustic events originating from xylem vessels allow for a wide array of use cases. One such use case is the non-invasive phenotyping of plants based on the geometrical properties of the vessels calculated using acoustic events. Using simple commercial integrated chips can be done in real-time as only standard signal processing tools are necessary. Other useable techniques include monitoring plants during drought-stress to observe the impact of drought on the viscoelastic properties of the vascular tissue and pathogen detection in the xylem vessels due to the changing kinematic viscosity.

This thesis will start with the state of the art from the literature in chapter 2. After this, we define the research question and objective in chapter 3. Having formulated the research question, the prototyping and fabrication process of the artificial structures is presented in chapter 4. In chapter 5, the method for the measurements and data processing will be presented. Using this method, the obtained results are presented in chapter 6. We will conclude the thesis with a discussion in chapter 7 and a conclusion in chapter 8 respectively. The appendices applicable to the main text conclude this thesis. After this, a manuscript for submission in The Journal of the Royal Society Interface, including appendices and supplementary, concludes this document.

Chapter 2

State of the art

This chapter presents the prior art relevant to the topic. The idea of this thesis is to study acoustic emissions from artificial plant structures. Therefore, it is first necessary to understand the biology of these structures in plants before we design our own artificial vessels. We will start with the structure of these xylem vessels in section 2.1. Then we study some artificial plant structures found in the literature in section 2.2. After this, we discuss the source of acoustic events we can expect to hear in (artificial) plant structures in section 2.3 and present the expected dynamics in section 2.4. Finally, we conclude this chapter with research into the literature on the fabrication of these artificial structures in section 2.5.

2.1 Biology

In order to understand the origin of the acoustic events, a solid understanding of the xylem vessel biology is required. A multitude of acoustic events can induce acoustic emissions inside the plant. An often measured location for these acoustic events is on the stem, with the louder recorded acoustic events originating from the fluid conveying xylem vessels of the plant [3]. Due to the biological differences between fluid-conveying vessels of different land plants [16], we will focus on the anatomy of the angiosperm species. This distinction is chosen for their prevalence in agricultural products due to their fruit-bearing characteristics.

We explain the basics of the fluid conveying structure of angiosperm plants with the help of figure 2.1 taken from Venturas et al. [16]. The shown structure consists of multiple shorter channels connected with perforation plates (remnant cell walls of the once alive cells). Different types of perforation plates exist, with two major types being simple perforation plates and scalariform perforation plates [17], shown in figure 2.2. The vessels are usually between 5 to 500 μm in diameter and are connected with tiny pits allowing for water transport between the different columns of channels [16]. Transpiration of water from the leaves at the top of the channels creates a pressure difference between the leaves and the roots, which, combined with the capillary action induced due to their small diameter, pulls up water against gravity and friction of water against the xylem walls [16].

In drought conditions, the tension on the vessels increases as water molecules evaporate from the leaves at a considerable rate, leading to a pressure gradient that puts the water column in the channels under a large amount of tension [16]. These pressure differences induce acoustic events when bubbles

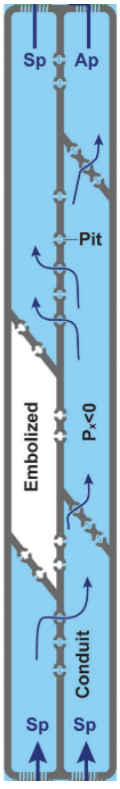

Figure 2.1: The fluid conveying xylem vessels, taken from Venturas et al. [16]

form, which releases the tension in the vessel while some of this energy is released as acoustic radiation [11]. These bubbles can then block the vessels as the air bubble prevents water from being pulled up, and the vessel becomes embolised [16], also seen in figure 2.1. As more and more of these events happen and vessels become blocked, the water supply to the leaves is broken, leading to damage to the plant and eventually mortality.

Different methods of bubble formation can be specified in the literature, with the most common occurrences when measuring acoustic events being spontaneous bubble nucleation and air-seeding [11]. Ponomarenko et al. [11] describes how bubble nucleation happens in wetted areas with no clear bubble source. In comparison, air-seeding, a phenomenon often described in the field of acoustic event measurements in plants, occurs due to gas bubbles travelling from an already embolised conduit to an operational conduit [18]. These bubbles must travel through the pits between the conduits, also shown in figure 2.1. The pits consist of a membrane of nanopores allowing water molecules to pass but preventing gas bubbles from moving through [16].

Currently, multiple hypotheses exist for these air-seeding phenomena, in which bubbles either move through the membrane as it stretches due to the high pressure exerted on it, the membrane ruptures or nanobubbles travelling through might coalesce into a larger bubble at the other side [19]. As a sufficiently large bubble has reached the fluid-filled conduit, the bubble will no longer be stable as it nucleates and grows until embolisation occurs [19].

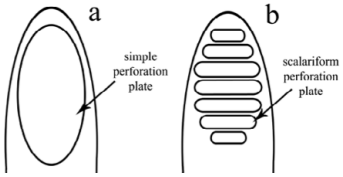

Figure 2.2: Simple and scaliform perforation plates that separate the xylem vessels in plants, taken from Wróblewska (2015) [17]

2.2 Artificial plant structures

Using the biology supplied in the previous section, we move closer to our goal of creating artificial xylem vessels by first studying those found in the literature. In 2008, Wheeler et al. [20] made an artificial plant structure using lithography. They carved microchannels into pHEMA sheets with a large surface area of channels functioning as the roots and leaves, creating a significant chemical potential between the two. This potential created a significant tension on the xylem vessel created from a single carved channel. Using hydrogel, they induced tensions of up to 1 MPa, while higher tensions resulted in vapour embolisms. Likely given reasons for these embolisms are the entry of contaminants or vapour nuclei into the vessels lowering the tension required for cavitation, which occurs in pure water around 21 MPa [20].

Another interesting artificial plant structure is presented by Guan et al. in 2006 [21]. In this paper, suction is applied on a microchannel using a relatively sizeable evaporative area in the form of filter paper clamped between a PDMS gasket with evaporative apertures. Using this filter paper, they created a pressure difference of 23.5 kPa allowing water to flow up the vessel. Another example of this method is used by Effenhauser et al. in 2002 [22] who used this method to create a continuous flow of 35 nl/min in 1 mm diameter tubes.

A third artificial plant structure was created by Shi et al. in 2020 [15], who connected 3 mm diameter tubes to a nanoporous ceramic disk to pull water up as observed in trees. Using this method, they transported water up the tubes to a height of 3 meters. The force pulling up the water inside the tubes is generated mainly by the Kelvin pressure, induced due to the mismatch in water activity between the subsaturated air above the disk and the saturated water inside the vessels.
In this paper, it is stipulated that the largest tension that a meniscus can generate in a conduit is given by the Young-Laplace pressure [15]:

$$P_L = \frac{2\gamma\cos(\theta)}{r_{pore}} \tag{2.1}$$

In this equation, γ is given as the surface tension, θ the contact angle of the pore and the liquid and r_{pore} the pore radius of the evaporative structure. This pressure must equate to the Kelvin pressure acting on the meniscus due to the mismatch in water activity between the air and water [15]. The Kelvin pressure is given by [15]:

$$P_K = \frac{R_{gas}T}{\nu_{liq}}\ln(a_{vap}) \tag{2.2}$$

In this equation, R_{gas} is the gas constant, T the temperature in Kelvin, ν_{liq} the molar volume of liquid water and a_{vap} the local activity of the water vapour above the meniscus. Usually, this pressure is higher in plants than the Laplace pressure [15]. To compensate for this, the meniscus in the plant retracts the meniscus until the local humidity adapts to a value that allows the Kelvin pressure to match the Young-Laplace pressure (Shi et al. (2019) [23]). Finally, Shi et al. propose three other important equations for water flow in their artificial plant structure. These three, shown below, are Darcy's law, the hydrostatic pressure drop and the Poiseulle equation, respectively.

$$\Delta P_D = \frac{Qt}{\kappa A}, \qquad \Delta P_H = \rho g H, \qquad \Delta P_P = \frac{8QH\mu}{\pi N R^4} \tag{2.3}$$

Darcy's law describes the estimated pressure drop over their wetted disk, while the Poiseulle equation calculates the pressure drop over the vessels. They state that these three pressure drops must sum up to the Young-Laplace pressure for mass to be conserved in their vessels.

2.3 Sources of acoustic events

Several studies can be found on the acoustic events (AEs) we can expect inside plant structures and our artificial structures in the literature. First, we discuss acoustic emissions observed in plants in section 2.3.1, then we discuss the acoustic emissions that have been observed in artificial tubes in section 2.3.2.

2.3.1 Plants

This section provides the findings of several important pieces of plant acoustics found in the literature. In the literature, many biological papers can be found on acoustic events originating from plants. Some essential early papers were presented in chapter 1 [2, 3, 18]. A more recent paper following the same method is one by Rosner et al. [4]. These papers all had a similar working method in which they related the cumulative acoustic events to the tension in the water column to obtain Sigmoid shaped plots. These plots take this shape as the tension needs to build up for acoustic emissions to occur. The emissions gradually increase until most vessels

have cavitated and the emissions drop off again. The cumulative acoustic events were measured directly on the stem in all these cases.

Ponomarenko et al. [11] took a new path and observed air-seeding with computed tomography, opting to use micro-CT (micro-computed tomography) in combination with recording acoustic events. By dehydrating thin slices of wood in hydrogel, they triggered acoustic events were in their samples. In this experiment, about 15% of visible events occurred in wetted areas, likely due to cavitation. They attribute the remainder of 85% of the emissions to air-seeding events. The cavitation events were more likely to produce a recordable emission, which might be due to the higher pressure differences of these events, with air-seeding generally requiring lower energy levels.

Subsequently, in 2015, Vergeynst et al. [7] inspected the wave propagation in branches by first modelling the branch as a PVC rod and inducing the pencil lead break technique on it to generate an impulse. By comparing the technique to dehydration-induced acoustic events, they speculated that "displacements during bubble growth, rather than superimposed small bubble oscillations of high frequency (...), may be a source of AE signals" (AE is an acoustic emission). Furthermore, they found strong attenuation of high frequencies in the wood by comparing near-field and far-field signals. They found these far-field measurements to have strongly discernible guided wave modes due to stem attenuation. In another paper by Vergeynst et al., a year later [9], they place more focus on waveform analysis and the frequency spectrum measured from acoustic events. Furthermore, elastic shrinkage was measured, which showed that high-frequency content (400-800 kHz) signals might result from capillary action of free water, microcracks and fast bark contraction. They also speculate that low-frequency content might originate from Haines jumps and macro-fractures while the medium frequency content ($\pm$ 100-300 kHz) was found to be most related to air-seeding and cavitation events.

In 2020, Oletic et al. [10] inspected the frequency characteristics of acoustic events with wide-band sensors. Starting at frequencies from 100 kHz to 1 MHz, they discerned three groups: Single component emissions, multi-component emissions and low-frequency broadband emissions. Single component emissions peaked around 200 kHz, while those of multi-component emissions ranged between 200 to 600 kHz.

One more recent study by Khait et al. [24] showed that we could also measure these acoustic events with a transducer placed at a ten-centimetre distance to the plants. This was utilised by Dutta et al. [12] in their experiment looking into the prediction of the vessel properties using the frequency spectrum observed from these acoustic events. We will go further into depth on their application in section 2.4.

2.3.2 Artificial structures

In artificial structures, hints at similar acoustic emissions can be found, even when no acoustics were measured. In their artificial vessels, both Wheeler et al. [20] and Shi et al. [15] observed embolisms of their vessels. Moebius et al. [25] did perform acoustic measurements in their study on porous media, recording a wide range of acoustic emissions. They observed several sources for the observed acoustic emissions in their media: Haines jumps, bubble entrainment, bubble oscillation, liquid bridge rupture, snap-off processes and grain collision.

These different events were shown to vary with different flow rates through the porous media and also with pore size. They observed how larger pores created fewer acoustic events than smaller pores. Furthermore, following the power law, the observed events in these larger pores were of lower power than those of smaller pores. Similarly to Moebius et al., Sun et al. [26] looked into pore-scale induced acoustic events as the fluid front moves. Several conditions for Haines jumps were studied: one in which an entrapped gas bubble was present in the system, one with a compliant solid matrix and one with interconnecting menisci. Haines jumps were

observed to occur more often in systems with a high pore constriction ratio, small contact angle and higher interfacial tension.

2.4 Structural and fluid dynamics

In this section, the formulas proposed in the work of Dutta et al. [12] will be explained and discussed. Acoustic emissions inside of the vessel will excite both fluid and structural modes, which we describe in the upcoming two sections.

2.4.1 Structural dynamics

Following Dutta et al. [12], we will use two different measurement directions with respect to the vessels: radial and axial directions. For an example on these directions, see figure 5.1. Radial measurements will have an acoustic propagation that includes extra attenuation by the solid wall thickness. Axial measurements are measured along the vessel and will mainly feel attenuation from the liquid and air, though the fluid-structure interaction also impacts them. The radial modes might find most of their attenuation by the flexural resonance modes of the xylem vessel structure. By comparing the vessel to a beam consisting of the composite of incompressible water and the xylem solid structure [12], we can use Bernoulli's beam theory to find harmonic frequencies. Assuming a circular beam surrounded by vascular tissue, we can write:

$$f_n = (\frac{k_n^2}{4\pi})(\frac{R}{L^2})\sqrt{\frac{E_{comp}}{\rho_{comp}}} \tag{2.4}$$

In this formula k_n represents the mode constant ($k_n = (n{+}0.5)\pi$ with mode numbers n=1,2,3,...), R the radius of the vessel, L the vessel length, E_{comp} the elastic modulus of the xylem vessel wall-water composite and ρ_{comp} the effective mass density of the xylem vessel wall-water composite.

We can expect influences on this equation by the perforation plates, which the formula does not take into account. Furthermore, this formula also does not include any fluid-structure interaction, which might cause a reduced natural frequency like modelled by França Júnior et al. [27], who compared flexural modes of an uncoupled cylindrical shell with that of a fluid-structure coupled shell. Similarly, using numerical simulation, the approximate composite structure could be compared to the fluid-structure coupled model to observe the frequency shift. Aside from the mode shapes Dutta [12] proposes, a radial settling time is defined by the damping provided by the solid viscosity: $\tau_{radial} = \frac{\eta_{solid}}{E_{vasc}}$. In this formula, η_{solid} represents the solid viscosity of the vascular tissue and E_{vasc} the vascular tissue Young's modulus. This radial settling time was found to be statistically similar to the axial settling time measured [12], which we will describe in the next section.

2.4.2 Fluid dynamics

By using axial detection, Dutta et al. [12] proposes the xylem vessels similarities to a cylindrical Helmholtz resonator. Their work found that the acoustic measurements extracted radii were in good agreement with microscopy measured vessel radii. For this, they used the following formula:

$$R = \sqrt{\frac{4\eta_l \cdot \tau_{axial}}{\rho_l}} \tag{2.5}$$

In this equation η_l represents the xylem sap viscosity, τ_{axial} the damping time of the envelope of the measured signal and ρ_l the sap density. Furthermore in the axial direction they propose acoustic resonance with flexible walls as the dominant wave propagation method, which results in resonance in the fluid. This gives the following equation:

$$f_m = (\frac{m}{2})\frac{\nu_{eff}}{L} \quad \text{with} \quad \nu_{eff} = \sqrt{\frac{(\frac{1}{K} + \frac{2R}{hE})^{-1}}{\rho_l}} \tag{2.6}$$

In this formula, m represents the mode number, ν_{eff} the effective speed of sound in water in the vessel, K the bulk modulus of the water and h the xylem wall thickness. Finally, for the axial resonance peak found in the signal, a frequency shift due to damping will need to be considered. This is taken into account using the following equation: $f_L = f_{p(axial)}\sqrt{\frac{1}{1-\zeta^2}}$, in which ζ is the damping factor of the pulse amplitude.

In these equations, the absorption of certain frequencies by the perforation plates in the vessels is not taken into account. While modelling the effect of all these plates is next to impossible in plants, their absorbing factor should be kept in mind. In a study of flexible micro-perforated plates by Temiz et al. (2017) [28], they found the influence of perforation plates to have a broad frequency-dependent absorption peak dependent on the geometry and material properties of the flexible plate.

2.5 Fabrication

Using the biological and physical background from the previous sections, we can create a first model of the xylem vessel. Assuming the most basic model of a cylindrical xylem vessel free to move and clamped on both sides, we will explore different fabrication methods in this section.

To fabricate the fragile artificial xylem vessels, we made several design choices. The fabricated material will have to mimic the properties of the xylem vessel itself. For this reason, the following material properties have to be considered: solid viscosity of the xylem wall, the Young's modulus, xylem vessel density and xylem contact angle. Looking at the density-Young's modulus plot (shown in figure 2.3A) of different materials taken from Gibson, 2012 [29], several options are visible to mimic wood and wood-like materials: Polymers, foams (ceramic, metal and regular) and composites.

We can design composites and polymers in such a way as to decrease the Young's modulus and density by creating porous structures. Foams would need to be designed for high Young's modulus and density instead. One study was found in the literature in which they used a composite silica frit to mimic the stem microcapillary structure. Wang et al. [14] used this in order to create a mangrove inspired desalination plant. The used frit was 2.2 mm thick and had pore sizes of 0.9 to 1.4 μm. Using a similar structure, however, would not be smart if the goal is to vary parameters, like xylem length and radius, as will be proposed in chapter 3. For that, we need a material that allows for the design of different porous structure sizes, which might still be out there but was not found in the literature. Similar problems would arise

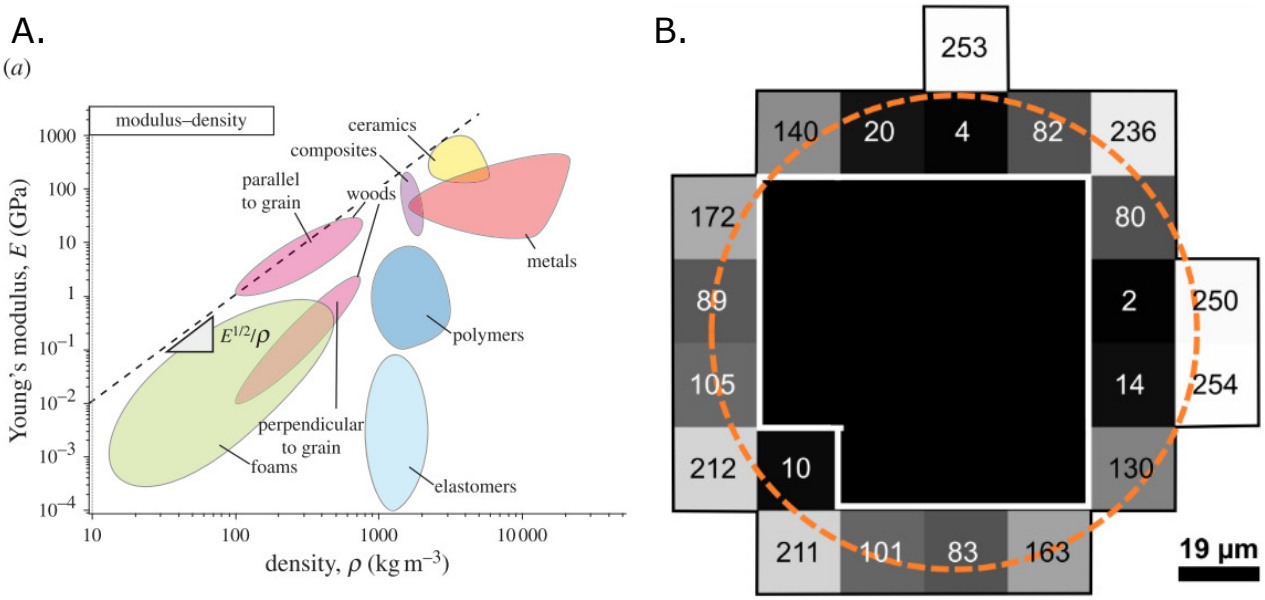

Figure 2.3: In figure A we see the Young's modulus versus density of different materials including wood parallel and perpendicular to the grain, taken from [29]. Figure B shows a voxel compensated 120 micron channel which was printed using a 19 micron pixel resolution printer, this figure was taken from Männel et al. (2019) [30]

for foams, where the fabrication is challenging to do in-house, but with manufactured goods, limitations are placed on possible geometrical properties. These limitations could be due to the budget or limited provided options by manufacturers. From the other materials, polymers can be 3D printed and moulded, which allows for strong control on geometry and density to find the best match with the xylem properties. Another option would be to use a mould of a different material, which could create a wide variety of materials. This, however, still requires a mould with the correct dimensions. One option for this would be to 3D print this mould.

Some geometric limitations occur due to resolution and minimum feature size, fabrication costs, and fabrication time for the fabrication aspect. Furthermore, not all fabrication methods work with the required material properties. 3D printing seems to be the best option as it is cheap, allows for solid parameter control, is relatively fast and in-house, with the downside of not always attaining the best resolution compared to alternatives. Within 3D printing, multiple printing techniques exist, with each their functionality. In order to mimic the microscale structure, a very high printer resolution is necessary. Within the field of 3D printing microfluidics, which seeks to attain similar low scale resolution channels as our xylem vessels, research has been done on which methods are best for 3D printing microscale fluidic elements.

In a review paper by Au et al. [31], the most suitable methods of microfluidics fabrication are named to be: selective laser sintering, fused deposition modelling (FDM), photopolymer inkjet printing, binder jetting, laminated object manufacturing and stereolithography (SLA). From this paper, the relevant conclusions are that 2-photon lithography printing is costly and slow but has by far the best resolution. Furthermore, only SLA and PolyJet printing attain resolutions of up to 20 μm, allowing for the required small feature design. Lade et al. [32], discusses another aspect of microchannels in their 2017 paper, inspecting the surface roughness of different printing techniques. They show how surface roughness for PolyJet printing without support generates a very different structure than with support. Both PolyJet printing without support and SLA printing showed a smooth surface. A stated problem of PolyJet printing without support was that the channel did not generate "well-defined" cross-sections deviating from the modelled channel.

Macdonald et al. [33] also compared microstructure channels, focussing on closed channels instead of planar open channels. This work compared 250 μm and 350 μm channels of fused deposition modelling, PolyJet and DLP printed structures. DLP printing, digital light processing printing, is a variation of SLA printing that prints by illuminating pixels in a resin bath, hardening them. In their work, the designs were printed horizontally and compared, with FDM printing suffering from its low resolution, PolyJet from support removal, but the best resolution and SLA printing was found to have the smoothest surface but suffered from collapsed walls due to underexposure. From Weisgrab et al. [34] most small resolution microfluidic prints can be seen to be printed using SLA printing. Many applications are shown, with most of these prints having 50 μm resolution and most having larger than 200 μm channels. In this line, Shallan et al. [35] managed to reliably print holes up to 300 μm with a 56 μm resolution printer. In this study, they also observed roughness at holes of unsupported features. All in all, SLA printing shows the most promise for the fabrication of our structure due to its smooth surface, good resolution and affordability.

In order to create microchannels under 300 μm in diameter, a thorough understanding of the printing process is necessary. Digital light processing printers work on the principle of micromirrors illuminating parts of the photopolymer vat curing it [36]. This is also shown schematically in figure 4.2A. Due to this working principle, the pixel size limits the resolution, with high-resolution commercial printers going down to 20-30 μm square pixels. Tiny enclosed microchannels might end up getting clogged by resin, as shown by Au et al. (2014) [37], where channels of 200 μm were fully clogged, and 300 μm were partially clogged. In their 2019 paper, Männel et al. [30] discuss printer parameters for creating microchannels in a working manner. They introduce the following guidelines for printing microchannels allowing us to print circular channels up to 120 μm in diameter with a 19 μm resolution printer:

- Firstly, printing should occur along the Z-axis as it results in less clogging.
- Secondly, the print should be lifted from the resin in between each layer to prevent clogging of entrapped resin.
- Thirdly, voxel compensation should be used to prevent clogging, which means the illumination should be varied pixel by pixel in a described manner.

Following these guidelines with our printer, the EnvisionTEC HD, the circular 120-micron diameter microchannel could be printed. For this, the illumination pattern in figure 2.3B would have to be used, taken from the supplementary of [30]. After printing, the channels were washed with IPA, treated in an ultrasonic bath, washed with demi-water, and post-cured [30]. If the microchannel is still clogged, we can use some techniques to unclog it. For this purpose, to clean their created square channels of 200 by 200 microns, Wicker et al. [38] used a pressure bomb of 10 MPa nitrogen on the channel. Gong et al. [39] managed to obtain even smaller microchannels with square channels up to 20x20 μm. However, they created their own 3D printer and tuned the resin to increase the resolution. Using layers of only 6 μm thick, they printed these channels horizontally, showing that even smaller channels could be created with proper printer design. Gong et al. [40] similarly managed to get tiny rectangular channels 50 microns high by altering the resin formulation.

Chapter 3

Research objective

In this chapter, we present the knowledge gap. We formulate the research question and subdivide it into objectives using this knowledge gap. In order to narrow down the goal of the research, some choices had to be made. Firstly, as described in section 2.1, we focus on the structural replication of angiosperm plants. Secondly, we chose the EnvisionTEC Micro Plus Hi-Res DLP type printer as the fabrication method with HTM140 V2 and 3D Tough Clear as the resins based on the findings from section 2.5. Using this printer, we place bounds on the model due to its XY resolution of 30 microns, which will only allow for replication of vessels above 120 μm in diameter (following Männel et al. [30] shown in section 2.5). Finally, the last focus will be on evaporation-based tension induction in the vessels as this method is easy to apply while replicating the biological method of inducing tension on the liquid column.

3.1 Knowledge gap

Using the theory supplied in the previous sections, we can identify some knowledge gaps. Firstly, statistical similarity was found by Dutta et al. [12] for the correlation between axial and radial settling times. This can be tested by concurrent axial and radial measurements on plants, which might reveal their correlation to become more clearly dependent or independent. Furthermore, in Dutta's work, the cause of overestimation of the length of the vessels is hypothesized to be due to the leaky boundaries. By adding or removing perforation plates to the artificial model, their impact on the estimation of the vessel length can be studied. On top of this, the perforation porosity could be varied to observe the influence on the acoustic response.

Another knowledge gap exists in the theorem on air-seeding and bubble nucleation in xylem vessels in general. Multiple hypotheses exist both about how air-seeding happens and what causes the spontaneous bubble nucleation measured by Ponomarenko et al. [11]. In a similar theme, the exact cause of acoustic events is also not fully understood, with possible causes being abrupt sources [7] like bubble nucleation and bubble oscillation [41]. Furthermore, the nature of the bubble as it emits the acoustic signal is unknown, with possibilities of them being cylindrical bubbles [42] and spherical bubbles [41], depending on the equilibrium radius and conduit diameter.

Knowing the exact source dynamics of the acoustic events might lead to a theory encompassing the entire dynamics from bubble nucleation to measured response. Furthermore, other events have also been hypothesized and observed to induce acoustic events, including events like water loss from other elements, macro-fractures, Haines jumps, and the likes [43]. These events might be acoustically recognized to discern them from the air-seeding events and obtain more information about the plant. Which of these other events occur in artificial microfluidic tubes has also not yet been documented to the best of the writers' knowledge.

Finally, more research is necessary on the predicted vibrational modes as proposed by Dutta et al. [12] and how they relate to the measured acoustic signal. The research question will mainly focus on predicting these vibrational modes and comparing them to the acoustic signal.

3.2 Research question

Using these choices and knowledge gaps, the research question and subquestions we defined are as follows:

How do the geometrical and elastic properties of 3D printed artificial angiosperm xylem vessels affect the dynamic characteristics of evaporation-induced acoustic events?

- Can an artificial 3D printed vessel replicate the acoustic spectra of a plant's xylem vessels?
- Which drainage effects can be observed in the artificial plant structure, and can we recognize them by their acoustic signature?
- Are the proposed formulae by Dutta et al. [12] applicable to the artificial structure, or do they need refinement?

Keeping these questions in mind, we will present the prototyping and fabrication of the artificial structures in the next section.

Chapter 4

Prototyping and fabrication

In this chapter, we discuss the prototyping and design choices of the artificial plant structure in section 4.1. After that, we explain the printing process of this artificial structure in section 4.2 and show the final structure. Finally, we also investigate the printing accuracy of the structure in subsection 4.2.1.

4.1 Modelling

In order to study the acoustics of the artificial plant structure, it is in our best interest to keep the geometry as simple as possible. The chosen geometry after multiple iterations can be seen schematically and as seen under the microscope in figure 4.1 with clamping areas marked in red. These multiple iterations were necessary to ensure the vessels did not clog, the orifices were well defined, and the wall thickness was sufficient to not break during printing. The thin walls of the final structure will allow for visual confirmations of the hydraulics inside the vessel as the material will be transparent, and the acoustics will not be as attenuated in the radial direction. In the end, both the 3DM Tough Clear and HTM140 V2 material allowed for visibility in the middle vessel element, with the 3DM material being more transparent than the HTM. This 3DM material allows for visibility in the clamped side vessels of the structure where the HTM140 V2 is no longer translucent.

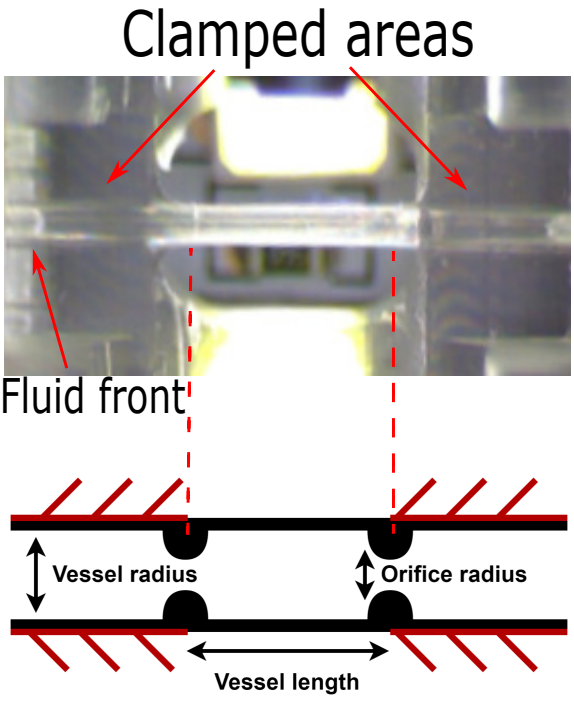

Figure 4.1: Schematic of the vessel shown on the bottom and the vessel as seen under the microscope on top. The locations of the orifices, clamped areas and the fluid front are shown

Looking at the model, we see one single vessel with orifices defining its boundaries on two sides. These orifices define three vessel elements, of which the solid structure around it clamps the two vessels on both ends, as seen in red in figure 4.1. This clamping allows for predictable flexural modes of the single free-floating vessel in the middle. The area surrounding the vessel protects the vessel against damage since the walls of the vessels are just 250 microns thick. The reference vessels are 5 mm long and have an inner radius of 0.25 mm. We varied this geome-

try from experiment to experiment while keeping all parameters except one fixed to study the influence of the varying one. Finally, the orifices have an inner diameter of 375 microns and a thickness of 300 microns. The geometry of these orifices can be seen in appendix A.

To induce dynamics in our system, we placed a piece of filter paper on one side of the vessel, similar to Guan et al. [21] and Effenhauser et al. [22] who used this to induce flow in their vessel. The filter paper placed on one side of the vessel mimics the plant's leaves due to their sizeable evaporative area and microporous structure resembling the stomata of the plant leaves.

4.2 Printing process

The structures devised in the previous section were modelled in Fusion360 and subsequently sliced to a printable format using the EnvisionTEC software Perfactory RP with a layer height of 50 microns. To prepare the print, we poured the resin into the resin bath through a filter to ensure no solid particles were present in the resin. Then the files were loaded, and we started the print.

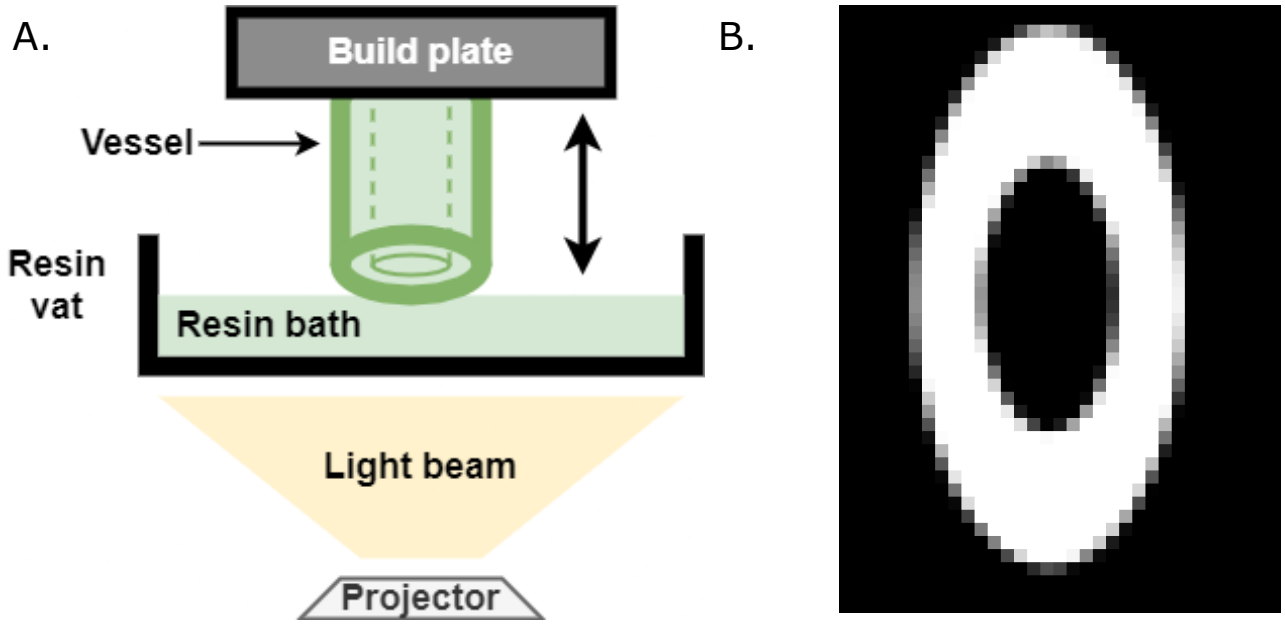

Figure 4.2: Figure A shows the DLP printing method, for each layer of 50 microns the sample is lowered in the resin bath and illuminated to harden the resin. Figure B shows one sliced layer of a printed vessel, along with the greyscale tints in the figure

For an overview of the printing method, see figure 4.2A. For each layer, the printer lowers the build plate 50 microns into the resin bath and illuminates the pixels of the shape we want to harden the resin locally. The sliced shape of one layer is shown in figure 4.2B, where white parts are illuminated with full intensity, grey areas with decreased intensity and black areas are not illuminated. These grey areas increase the smoothness of the print, as was also shown in figure 2.3B.

After printing, the structures were washed in IPA for 7 minutes using an ultrasonic bath (Bandelin Sonorex RK31). Then we dried the structures and cleaned the tubes using a pump supplying 2 bars of pressure. Subsequently, we removed the support from the print, washed the structures for 7 minutes and cleaned them again using a pressure of 2 bars. Finally, we cured the structures in a Dentalfarm Photopol Light Curing unit using UV cold light bulbs for 3 minutes and UV spots for 3 minutes.

4.2.1 Printing accuracy

Before we created full vessel samples like shown in figure 4.1, we performed some tests on the accuracy of the printing method. Since the radius variation is difficult to print, we printed different hole sizes to observe the difference between printed diameter and modelled diameter. The result of this experiment can be seen in figure 4.3A. The modelled diameters were as follows, starting from the top left: 1000, 800, 600, 500, 450, 400, 350, 300 and 250 μm. Looking at the results, we see that the printed diameter is close to the modelled diameter. We also did another experiment with smaller diameters. However, this experiment resulted in clogged channels, probably due to the resin not flowing out of the channel and slowly hardening during the print. After verifying the range of diameters, the orifices were test printed. The orifice parameters were varied and observed using a cut open version of a tube with a vessel in it; for an example of the final orifice geometry, see figure 4.3B. An orifice thickness of 300 μm (6 layers) and a diameter of 187.5 μm was chosen. We chose this diameter as it was one of the smallest printable orifice diameters. Thinner orifices would often fail to print or clog the vessel, which stopped happening for our chosen thickness of 300 μm.

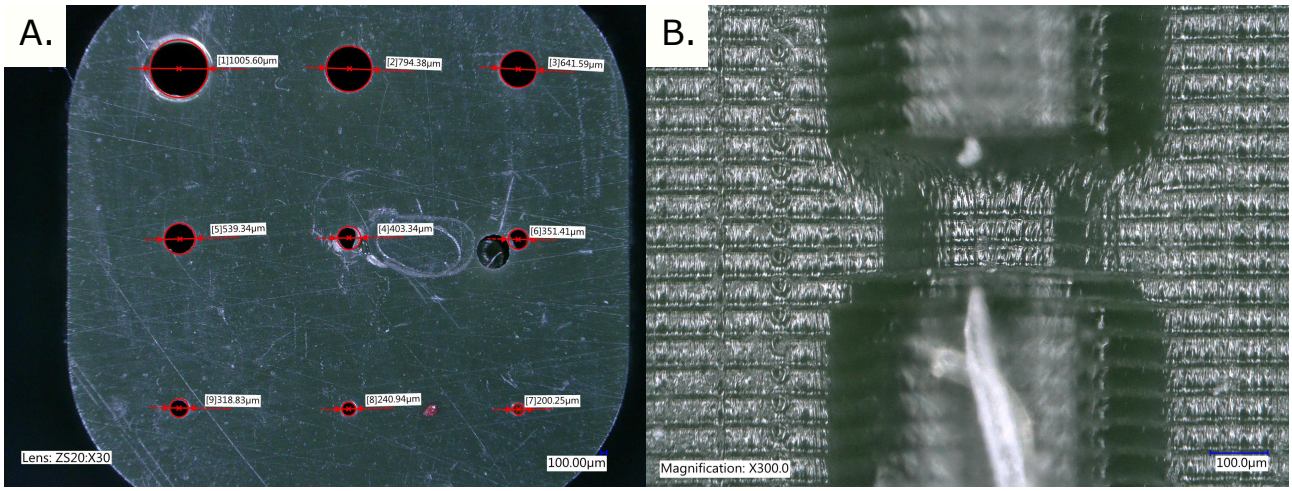

Figure 4.3: In figure A we see the accuracy of the printed holes (Modelled with diameter of: 1000, 800, 600, 500, 450, 400, 350, 300 and 250 μm). In figure B the cross section of an orifice in a vessel of 250 microns wide is shown (orifice height is 300 μm, its pore diameter is 187.5 μm)

Chapter 5

Method

In this section, we present the methodology used for this thesis, starting with the setup for the measurements in section 5.1. After that, we present the process of conducting an experiment in section 5.2, and explain the subsequent data processing steps in section 5.3. Finally we describe the numerical model in section 5.4

5.1 Setup for the acoustic measurements

After printing and hydrating the artificial plant structures, the xylem vessels are ready for acoustic measurements. The setup we used to perform these experiments is shown in figure 5.1 while a picture of the entire setup can be found in appendix B with all the used equipment listed.

Due to the low pulse amplitude of the acoustic emissions from our artificial plant structure, we created an anechoic box covered in acoustic foam. This box also functions as a way of keeping unwanted pulses away from the measurement. Furthermore, this acoustic box reduces the background noise inside the box, leading to a higher signal to noise ratio. Both acoustically with a microphone (Batsound M500) and optically with a microscope (2.0M Pixels digital microscope USB), the vessel, shown in red, is observed. Acoustic events with an amplitude above 0.035 a.u. in the axial and 0.015 a.u. in the radial direction on the microphone will trigger the recording, saving the data 0.2 seconds before and up to 2 seconds after the trigger occurred. The reason why we chose these values will be explained in section 6.4.1.

During humid weather, water evaporation from the vessel was very slow, and we decided to control two factors that impact this evaporation. This was done by increasing the temperature and decreasing the humidity of the air inside the acoustic box. We increased the temperature in the box using a 40W incandescent light bulb from Philips, while a Pingi car dehumidifying pouch decreases the humidity inside the box. Finally, a USB data logger monitors the temperature and humidity in the box. For more information on the setup, see appendix C.

Aside from the measurements performed with this setup, we also inspected the Young's modulus of the 3D printed materials. We did so by tensile loading tensile test strips printed along the Z-direction of the 3D printer and measuring the elongation and stress applied on the material. The process and results are shown in appendix D. We found the Young's modulus for the HTM140 V2 structure to be 1.56 GPa while that of the 3DM structure was 1.84 GPa.

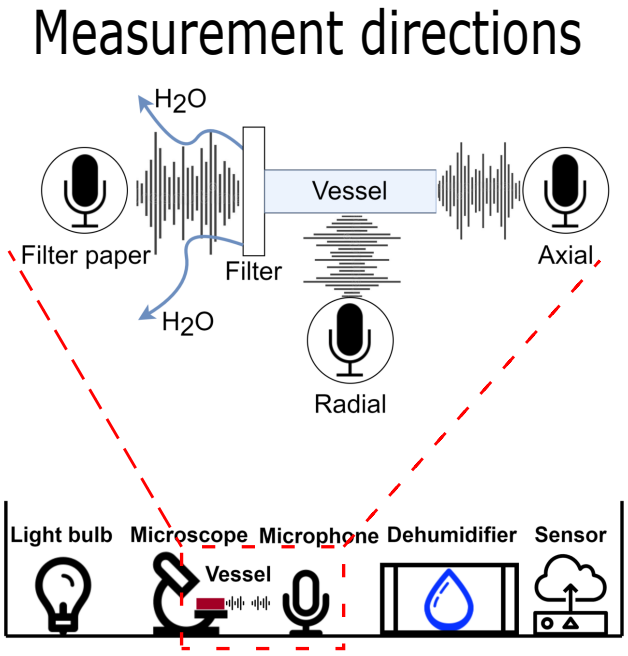

Figure 5.1: Schematic of the experimental setup and the measurement directions on the vessel along with the location of the filter paper. A picture of the setup can be found in appendix B

5.2 Experimental procedure

Before starting an experiment, we placed the artificial structures submerged in water to ensure the vessel was hydrated. We started the experimental procedure by sucking water up the vessels through a straw to make sure the vessels were fully water-filled and subsequently checking the vessel to ensure no bubbles existed inside it. After this, the filter paper was placed on the vessel while still wet with two caps pressing the filter paper on the structure. Then we placed the artificial structure inside the box under the microscope. For the measurements, we used the microphone to measure on three sides: on the filter paper, in the axial direction and in the radial direction. Using two microphones, we measured on all three combinations of these directions. For a schematic of this, see figure 5.1.

Having positioned the vessel, we started the temperature and humidity sensor and placed it inside the box. An example of the readings can be seen in figure 5.2A. After this, we started the microscope and microphone and closed the lid. Finally, we turned on the for 25 minutes and observed through the microscope.

For the first set of measurements, looking into the nature of the acoustic emissions, we performed measurements until there had been no acoustic emission for 1 hour or the vessel had been fully drained. For later measurements with varying parameters, the measurement was stopped after 2 hours as most acoustic events will have occurred by then, regardless of whether the vessel is fully drained yet. After finishing the experiment, we saved all the data, which will be further processed in the next section.

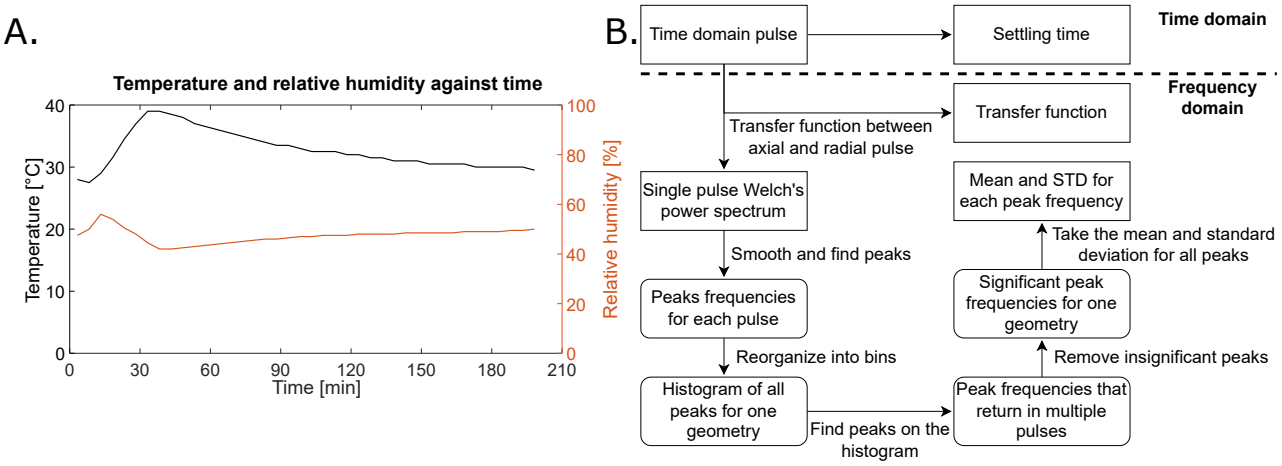

Figure 5.2: Figure A shows the fluctuation of the temperature and humidity inside the box during a measurement. Note the 25 minutes of heating and its large impact on the humidity. In figure B we show a flowchart of the method used to process the data. For an example on each step see figure 5.3

5.3 Data processing

Multiple experiments had to be done for some geometries to obtain enough data points. We saved the triggered acoustics in a separate folder as a .wav audio file for each direction. This file was loaded into Matlab using the *audioread* command. This function gives the amplitude of the pulse for each sampled point. The first 50000 data points are assumed to be not excited as these occur before the peak (this is nearly always the case). We used these data points to calculate the noise level for each pulse, an example of which can be seen in figure 6.3. Subsequently, we found the peak for each pulse and used the 1000 data points before and 5000 data points after the peak for further studies. This data was then trailed by 4000 zeros to zero pad the signal. Finally, we saved the original maximum amplitude of the pulse and normalized the signal in the time domain to compare power spectra in the frequency domain more easily.

Using the now available pre-processed time-domain data, the timestamps of the pulses were compared in the axial and radial direction to find synchronous pulses. We noted the time offset between the two microphones and denoted pulses occurring within 0.1 seconds of each other and showing similar dynamics as synchronous pulses. Finally, on this time-domain data, the settling time is calculated using a logarithmic fit on the envelope similar to Dutta et al. [12] and saved. This settling time, together with the pulse amplitude, was used to distinguish the synchronous pulses into three types of pulses. This distinction will be described in section 6.3.

5.3.1 Conversion to frequency domain

In order to inspect the power spectrum of the pulse, we used the Welch's power spectrum of the triggered pre-processed time-domain pulses. We calculated this spectrum using the `pwelch` function with a Hanning window and a window length of 2500 samples in the time domain. Furthermore, we dictated an overlap of 50 % and a sampling rate of 500000 samples per second (inherent to the microphone) for this function. Finally, we converted the results to Decibel. These power spectra will be further processed to find modes for each geometry in the next section.

In order to cross-check the results, we calculated the transfer function between the axial and radial directions. This transfer function highlights the difference between the power spectrum of axial and radial pulses, confirming whether the observed trends make sense. The transfer function is calculated in Matlab using the `tfestimate` function. For this function, we used the

same setting as used in the `pwelch` function and subsequently also converted this spectrum to Decibel. These results were then plotted against the pulse index and frequency to create the final spectral colour maps.

5.3.2 Finding modes

In order to find the mode frequencies in a large sea of different pulses with possibly different origins, we devised a new method. Our method looks at peaks that often occur among the different pulses of each geometry to find likely eigenmodes of the vessel. A flowchart of the used method can be found in figure 5.2B, while figure 5.3 shows an example for each step of data processing.

Having obtained the Welch's power spectrum for every pulse, we used the MATLAB `findpeaks` function on the smoothed spectrum (span 5) with a minimum prominence of 5. Subsequently, we converted all the resulting peaks for all pulses of the chosen geometry in one direction to a single histogram with bins of 3 times the frequency resolution of the power spectrum. This histogram is the number of peaks counted per frequency of all pulses for one single geometry. Therefore, if we observe a peak at the same frequency in a multitude of pulses, this peak is likely caused by the attenuation of the vessel. Thus, if we have peaks on this histogram they likely tell us the mode frequencies of the vessel. Using this notion, we found peaks on the histogram, again using the `findpeaks` function, with a minimum prominence of 1. We filtered out peaks with a more negligible probability as these are less likely to be important modes. The resulting peaks were taken as our observed eigenmodes. Using these eigenmode frequencies, we take all peaks within 3 kHz of the general peak of the studied geometry to calculate the mean and standard deviation for each found mode. This 3 kHz was chosen based on tolerances obtained in section 6.5.1.

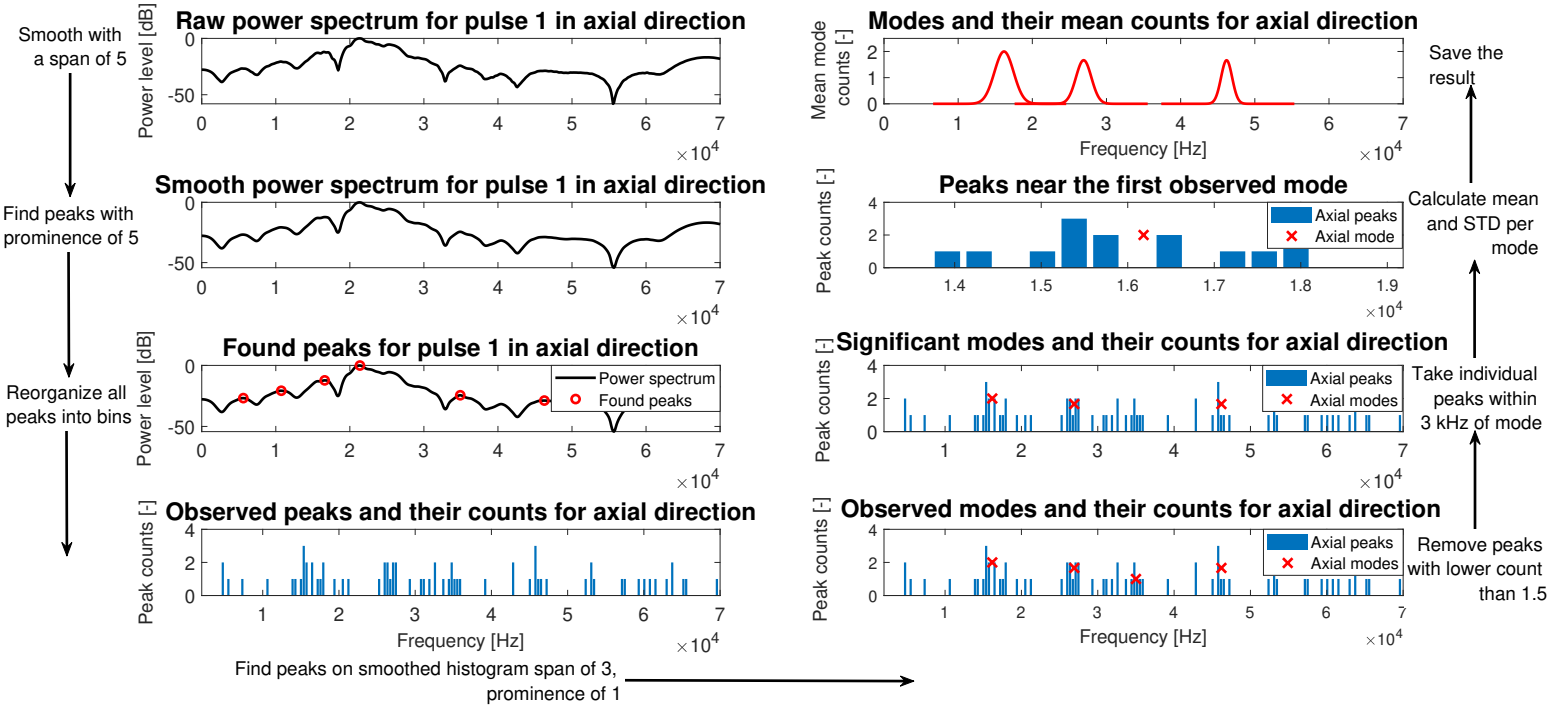

Figure 5.3: Method for finding overall mode frequencies per geometry, each step is highlighted. We start with the power spectrum obtained using the `pwelch` function. Note the removal of one axial mode between step 5 and 6

5.4 Numerical simulation

For the numerical simulation, COMSOL Multiphysics was used to model the eigenmodes of the vessel. We used two COMSOL physics in these studies: Solid Mechanics and Pressure Acoustics, Frequency Domain. These were coupled using the Acoustic-Structure boundary multiphysics. We then replicated the geometry to be similar to the modelled geometry and meshed it with a finer setting mesh. We used an isotropic linear elastic material for the Solid mechanics to simplify the model. This can be expected to introduce some margin of error to the results as, in reality, 3D printed material is highly anisotropic. We then fixed the boundaries marked in blue in figure 5.4 in the Solid Mechanics physics, which corresponds to the red areas highlighted before in figure 4.1. In the Pressure Acoustics physics, we modelled the internal fluid-structure boundaries as Sound Hard Boundaries, while we modelled the fluid-air interface at the two ends of the vessels as Sound Soft Boundaries. Using a parametric sweep over the length and radius, we generated the results with the eigenfrequency solver between 1 and 70 kHz. The results of this study will be presented later along with the experimental results in section 6.6.

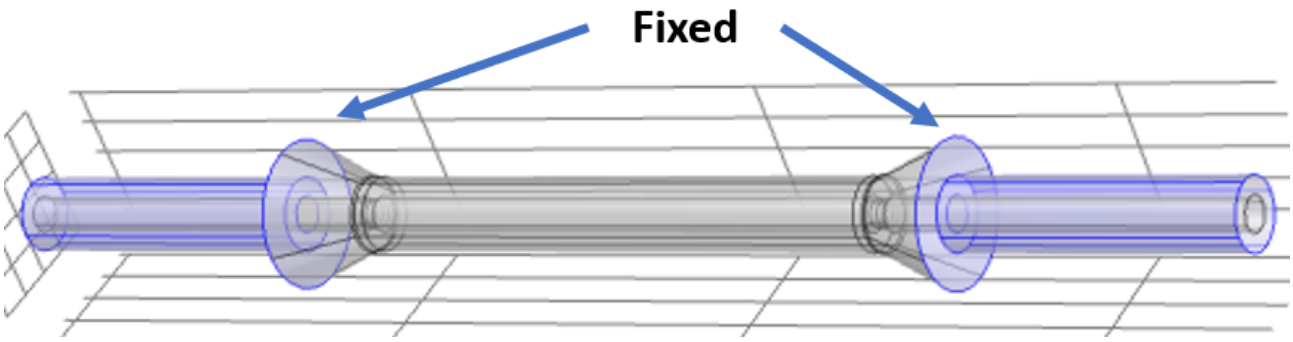

Figure 5.4: This figure shows the clamping points of the vessel. These areas are "fixed" inside the solid 3D printed structure

Chapter 6

Results

In this section, we will discuss the results, starting with an investigation into the evaporation of water from the structure in section 6.1. Moving on, we study the drainage behaviour and try to find synchronous optical and acoustic events in section 6.2. Subsequently, we inspect the waveforms we observe from the vessel and categorise them into three types in section 6.3. Using this, in section 6.4 we find sources for the acoustic events. Finally, we move on to the results of the geometry variation experiments by first simulating them using COMSOL in section 6.5 and then comparing them to the experimental results in section 6.6.

6.1 Evaporation studies

While performing the first acoustic experiments, we observed most acoustic pulses during the first hour of the experiment. We further studied this behaviour by simultaneously measuring the mass of the entire artificial structure, observing the vessel under the microscope and measuring acoustic pulses axially. The results are shown in figure 6.1A.

We found that most acoustic events occur during the rapid decline of the mass of the artificial vessel structure. Using the microscope, we estimated the mass of the water inside the vessel using its known volume and added the mass of the dry vessel structure to this. This estimated mass is shown in light blue in figure 6.1A. We observe the linear and slow decrease of mass of the water inside the vessel using this method. Since the mass of the water inside the vessel decreases linearly while the mass of the artificial structure decreases very rapidly in the first 90 minutes, many acoustic events in the 90 minutes are likely to originate from other sources than inside the vessel. The measured mass also slowly decreases after this initial stage, seen on the right side of the black line in figure 6.1A. After about 4 hours, most acoustic events have happened while the fluid front slowly recedes for about 6 hours until it fully embolises the vessel. Sources of acoustic events could include the filter paper, heating of the material and surface evaporation. These sources will be further studied in section 6.4.

After the black line, we have an approximately linear mass decrease in the vessel. Calculations on the volume flow rate of water out of the vessel after this point show 6.37E-14 m^3 of water evaporate every second. Using Darcy's law and the Poiseulle equation shown in equation 2.3, we can estimate the pressure losses in the vessel if it were functioning as a tree. From Darcy's law, we obtain, using the same material properties as Shi et al. [15] used for their disk and the calculated flow rate, a pressure drop of 7.4E-3 Pa over the filter paper. Using the Poiseulle equation, we find a pressure drop over the vessel of 5.5E-4 Pa. These pressure drops are very small, though the flow we could induce using this artificial structure is limited as well. An increase in flow rate would induce larger pressure drops.

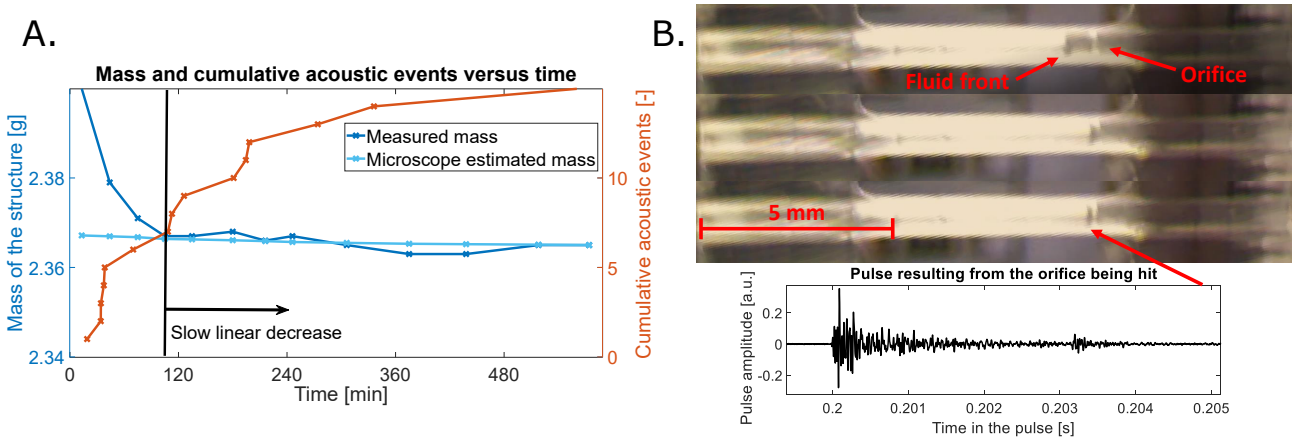

Figure 6.1: In figure A the evaporation rate of mass in the vessel is shown. After the black line most of the mass outside of the vessel has evaporated, yet acoustic emissions still occur. In figure B we show the synchronous acoustic emission and optical event. An acoustic emission occurred as the fluid front hits the orifice. The resulting acoustic emission is shown below the optical event

6.2 Microscope studies

Now that we have an idea of the evaporation of water from the structure, the next step is to look further into the drainage effects in the vessel. We start by estimating the time difference between the microscope and microphone.

6.2.1 Time difference

We observed an easily visible event that produced an acoustic emission during measurements on the surface evaporation of water from the 3DM Tough Clear material. The microscope frame rate is known to be 29.41 frames per second. Comparing the time stamp of the acoustics to the frame the event occurs on the microscope, the time difference is observed to be less than 0.05 seconds. Therefore, when events occur within 0.1 seconds of each other, there is a high probability of the microscope and microphone observing the same event.

6.2.2 Observed events

We used the 2.0M Pixels Digital Microscope to observe macro-scale events inside the vessel. Drainage of the vessel occurred as follows: the fluid front recedes from the microphone side to the filter paper until the orifice traps it temporarily. Here it gathers enough tension to continue draining and then fully drains the vessel after passing the next orifice. During these experiments, we observed bubbles in the vessel in a few cases. When they appeared, the fluid front subsequently entrained them. Perhaps those bubbles that did appear might be similar to Shi et al. [15] due to improper charging of the vessels. In one case, we found an optical event synchronised with an acoustic emission, shown in figure 6.1B. Here the fluid front reaches an orifice inducing the pulse seen below the pictures of the vessel.

Aside from this synchronous event, many optical events occurred which we expected to carry an acoustic response that did not create any observable emissions. One such event occurred as the fluid front reached an orifice, touched it and snapped back 1 millimetre in a fraction of a second. Perhaps the acoustic power was not high enough for these events as the signal was too attenuated to trigger the microphone. Another event that we expected to create an acoustic emission was the entrainment of bubbles by the fluid front. Following Moebius et al. [25] this might have induced an acoustic event, but it was most likely too weak in power to detect by the microscope.

Except for the one synchronous event of figure 6.1B, on a large scale, it can be said that fluid front displacement does not result in any acoustic emissions of sufficient acoustic power. Nevertheless, we still observed many pulses without any visible accompanying event. The most likely cause is that the microscope does not zoom in enough to observe microscale events like Haines jumps or the acoustic events inside the filter paper.

6.3 Waveform analysis

We identified three types of pulses from their time-domain characteristics during the experiments. These pulse types are shown in figures 6.2A, B and C, respectively. The first of these types has dynamics too fast to capture with the Batsound M500 microphone (250+ kHz) and a fast settling time of about 50 microseconds. Due to these fast dynamics, the frequency spectrum is featureless. The second type of pulses we observed, shown in figure 6.2B, have the highest amplitude on average, a settling time around one millisecond and discernible peaks between 5 to 70 kHz. The settling time of the third pulse-type was longer, and its power spectrum focused more on lower frequencies. For an example of the frequency domain spectra of these three pulses, see figure E.1 in appendix E.

In figure 6.2D, the distinction between pulse types two and three becomes visible when plotting the settling time against the pulse amplitude. Furthermore, an exponential fit seems to work quite well for both pulses, though this is likely the result of the method used to calculate the settling time, as will be explained in chapter 7. Finally, type 1 pulses are left out in this plot as their settling time is an order of magnitude smaller. These pulses would all be concentrated in the left bottom of the figure.

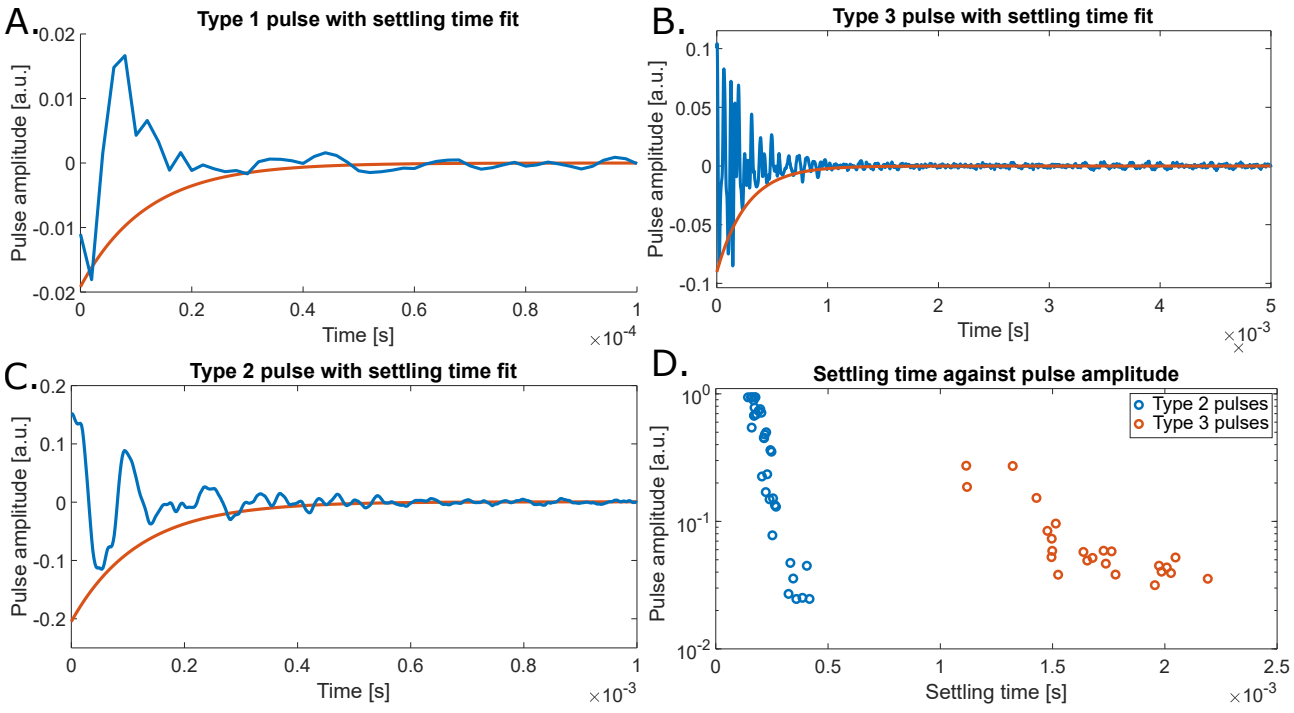

Figure 6.2: Figure A to C shows the time domain of the three pulse types and their logarithmic fit. Figure D shows the settling time versus amplitude (logarithmic) for the type 2 and type 3 axial pulses highlighting the clear distinction between the two types. Type 1 pulses are not shown due to difficulties obtaining their short settling time, they would be located in the left bottom

6.4 Acoustic sources

Before we move on to the main results, the noise and acoustic sources in the system should be understood. In this chapter, we will start with the background noise. Once this is quantified, we study different sources of pulses and form a hypothesis on their origin.

6.4.1 Background noise

While performing initial measurements, we noticed how events like moving a chair triggered the microphone. To prevent these unwanted sources of acoustic events from triggering the microphone, we created an anechoic box. This box also brings down the acoustic power of the background noise, which now peaks around -110 dB, as can be seen in figure 6.3. This figure also shows the microphone's characteristics quite well with its steep drop off below 10 kHz. As soon as we turn on the electronics inside the setup, we observe some additional noise. The primary source of noise with a peak between 44 to 48 kHz is the light bulb, yet this noise is filtered out using the Hanning window. We decided to turn the trigger of the microphone to an amplitude of 3.5 % in the axial direction, as stated in section 5.1. This corresponds to a power level of -29 dB, meaning only significant pulses trigger the microphone. Since the radial direction generally has weaker pulses, we set its trigger to 1.5 % (-36 dB). While inspecting the acoustic power of a pulse, we compare the power level of the pulse to that of the noise by taking the first 0.1 seconds of the pulse as this part of the signal is usually not excited.

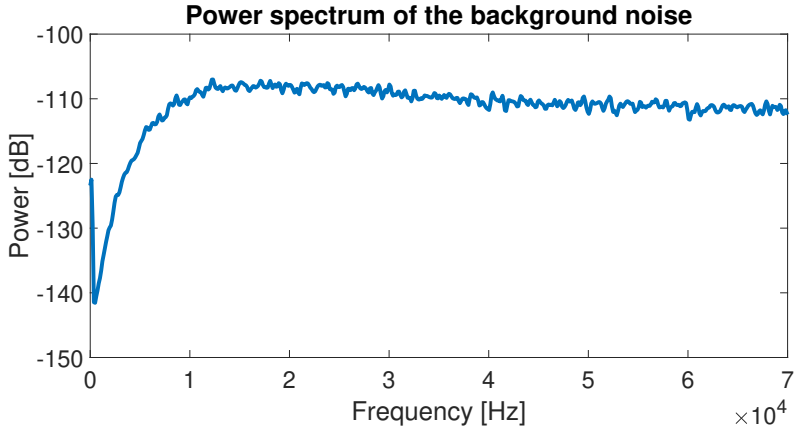

Figure 6.3: Background noise inside the anechoic box with the light bulb switched on. Without windowing a peak caused by the light bulb is visible around 44 kHz

6.4.2 Acoustic sources

We then started looking into sources of acoustic pulses within the box. Knowing different sources is essential as not all sources will have their signal attenuated by the vessel, meaning their frequency spectrum is uncorrelated to the vessel's geometry. We performed the following experiments to observe different sources for these pulses:

(A) Heating of an oven-dried vessel structure
(B) Evaporation of water from the filter paper
(C) Acoustic events induced in a drained vessel
(D) Evaporation from a water filled tube without any filter paper or heating

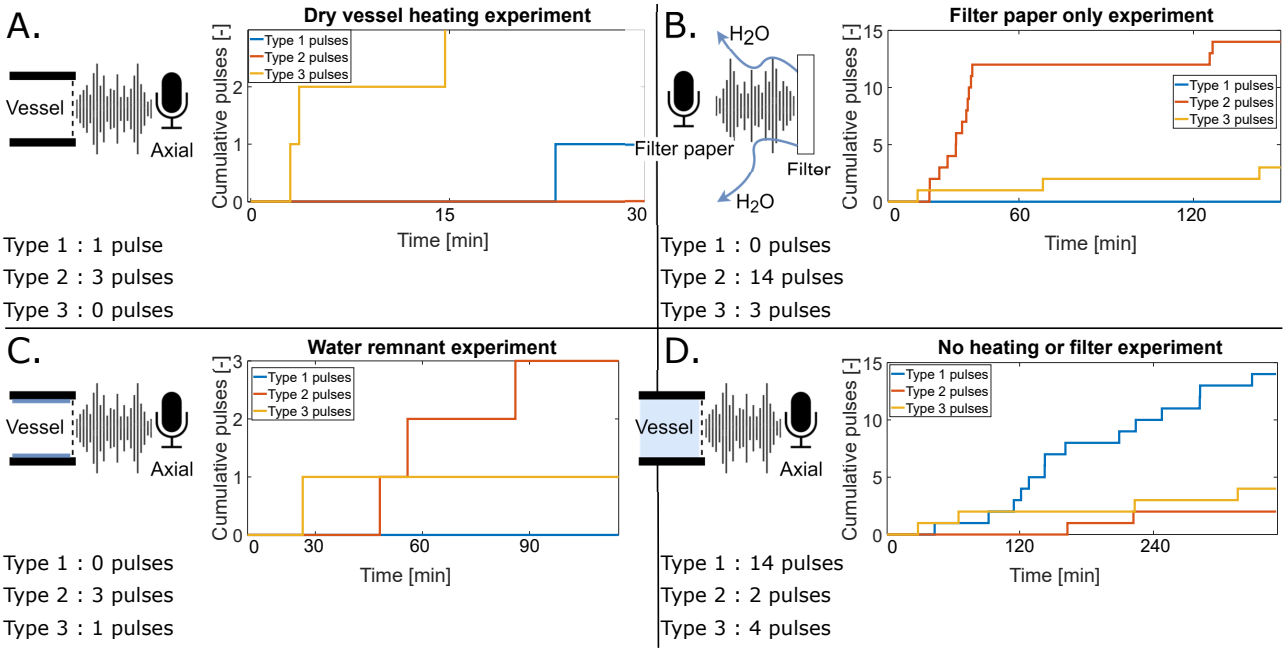

Figure 6.4: The four performed experiments on sources of acoustic emissions: heating a dry vessel, the wet filter paper, remnants of water in the vessel and the vessel without heating or filter paper. For all experiments we used a structure with a vessel length of 5 mm and a radius of 0.25 mm

These sources can be seen in the same order in figure 6.4. Starting with experiment 6.4A, we dried a vessel in the oven to ensure there was no water left inside the vessel. After removal from the oven, the only water in the structure could be due to the formation of monolayers. When we placed the vessel in the box and elevated the temperature with the light bulb, we observed four pulses. Three of these pulses had the slower type 3 pulse characteristics, while one pulse was of type 1. The origin of these three pulses is likely quite similar as their frequency domain characteristics were also similar. These type 3 pulses most likely originate due to the expansion of the 3D printed material. One way this could induce acoustic emissions is by the formation of microcracks. This thermal-induced microcracking leading to acoustic emissions was something observed in ceramics by Srikanth et al. [44].

We found a significant source of acoustic emissions to be due to the evaporation of water from the filter paper, shown in figure 6.4B. In this experiment, we observed 14 type 2 events triggering the microphone in just 75 minutes, with the majority occurring in the first 30 minutes. Correlation in the frequency domain for these pulses was lacking, although they most likely originate from similar sources. One source for these events could be Haines jumps, as seen by Moebius et al. [25]. Haines jumps occur as the fluid front in the paper suddenly jumps from one pore to the next as the paper dries. The uniqueness of the frequency content might be explained by the unique nature of these pores, as the filter paper consists of fibres. Aside from the type 2 pulses, we also observed three type 3 pulses.

The third experiment, shown in figure 6.4C, shows acoustic events still occur inside drained vessels. In this experiment, we filled a vessel, drained the water column inside and immediately placed it next to the microphone. The result is an air-filled vessel with a layer of water on the surface inside the vessel, which could emit acoustics while drying. We observed little pulses during this experiment; Within 105 minutes, we observed three type 2 pulses and one type 3 pulse. One source could be the relaxation of the surface tension of water trapped in microscopic imperfections in the 3D printed structure.

Finally, the last experiment shows how taking away the sources shown in figures 6.4A and 6.4B, still leads to a significant amount of acoustic events originating from the structure. This experiment, shown in figure 6.4D, was performed on a fluid-filled vessel without heating from the light bulb or the use of filter paper. This experiment shows how type 1 pulses originate from inside the vessel. We also see how type 2 and type 3 pulses occur without heating or filter paper, albeit in a limited amount. Finding exact sources of acoustic emissions in these cases is difficult. Sources could include: Haines jumps, snap-off of the fluid front, bubble entertainment or oscillation, and liquid bridge rupture as discussed by Moebius et al. [25].

To conclude these experiments, we inspected pulses from the evaporation of water from the surface of a 3D printed structure. In one experiment, we observed no pulses, while in the second experiment, we observed two type 3 events. These events were also visible on the microscope and occurred due to the snapback of water on the surface. These pulses can be recognized with the microscope and filtered out during the experiments.

6.4.3 Unique filter paper acoustics

We observed some very sharp acoustics while measuring directly on the filter paper. Shown in the top plot of figure 6.5, these pulses reach peak amplitude quickly and subsequently damp without any form of oscillation. These pulses did not occur while measuring in the axial or radial direction. When we measure the response of this pulse on the axial side, we see it has shifted into an oscillation. The origin of this damped pulse and its subsequent transformation into an oscillation remains elusive.

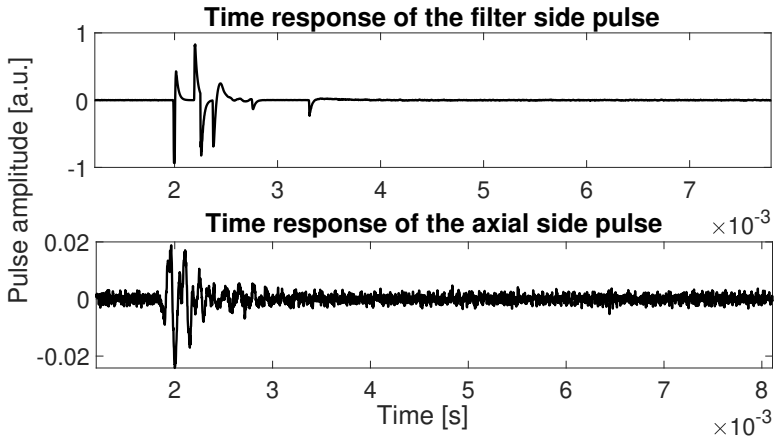

Figure 6.5: An acoustic emission with sharp characteristics as measured from the filter paper is shown in the top plot. Shown below is the same pulse as measured on the axial side of the vessel

6.5 Numerical studies

This section shows the impact of varying the vessel length and radius on the predicted eigenmodes using numerical simulation in COMSOL Multiphysics. These studies will provide good comparison material for the experimental results and predict the trend in the frequency shift observed for different vessel lengths and radii. A description of the numerical model was provided in section 5.4.

During the inspection of the numerical results, we observed the impact of the orifices to be quite large. An example of the first two orifice induced modes can be seen in figure 6.6. Note the large displacement visible around the orifices of the vessel. The orifice mode frequency shifts down slightly with both increasing vessel radius and length. The flexural modes of the vessel for length variation follow the same trend as shown by equation 2.4 proposed by Dutta et

al. [12]. For the radius variation, however, the flexural mode slightly increases in frequency up to R = 0.7 mm and suddenly goes down again above this value. None of these flexural modes was observed in the experimental data, as will be shown in section 6.6. In this section, we plot the numerical simulation and experimental results together in figures 6.8 and 6.11.

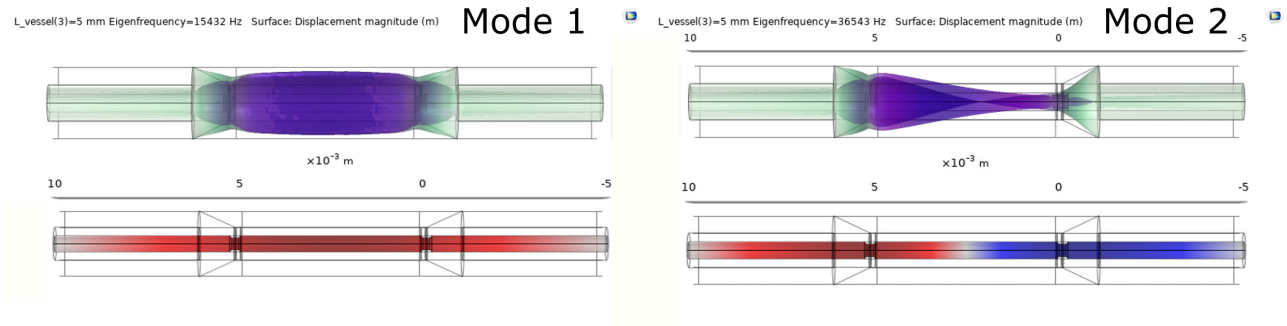

Figure 6.6: Example of the orifice modes as observed in COMSOL. The top figure shows the solid displacement which is coupled to the acoustic pressure shown below it. These examples are taken of the reference structure of L = 5 mm and R = 0.25 mm

6.5.1 Tolerances

In section 4.2.1, the accuracy of the printing was studied where we observed a maximum deviation of approximately 6%. Using numerical simulation, we studied the impact of these fluctuations in printed geometry. Taking a safety margin, we modelled the structure for a 10% change in length and radius for the reference geometry (L = 5 mm, R = 0.25 mm). The resulting eigenmode frequencies can be seen in figure 6.7A and B, with a maximum deviation of less than 1 kHz for the radius variation and up to 3 kHz for the length variation measurements. This 3 kHz was also used as the area in which we look for peaks around found eigenmodes in section 5.3.2. We calculate the mean and standard deviation for the experimental results using these peaks.

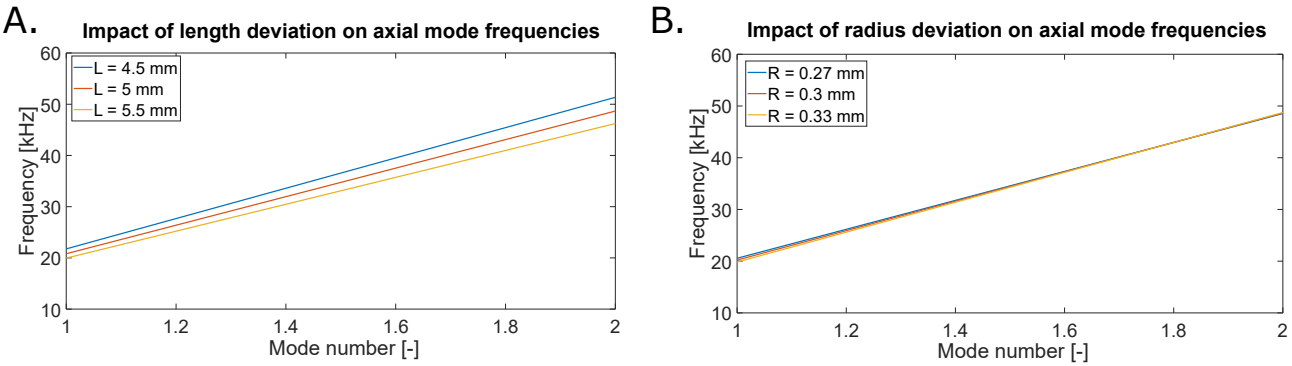

Figure 6.7: Impact of a 10 % deviation in vessel geometry on the two orifice modes. Shown in figure A we see the length variation measurement, in figure B we see radius variation

6.6 Geometry variation - vessel length and radius

Having studied the multitude of possible sources of acoustic events and the predicted numerical eigenmodes of the vessel, we varied the vessel length and radius. The results obtained by following the methods described in chapter 5 are presented in this section, starting with the length variation experiments.

6.6.1 Length variation

Firstly, we varied the length of the vessel to inspect its impact on the eigenmodes we find using the method proposed in section 5.3. We compare the results from this method in the axial and radial direction to the orifice modes we observed from the numerical results in figures 6.8A and B. All found experimental modes are plotted, showing the significant difference in the number of peaks found between experiments. Furthermore, clear trends in the data are shown in red. Since we modelled the Young's modulus in COMSOL as an isotropic material while, in reality, DLP printed structures are highly anisotropic [45], we can expect some margin of error. We scaled the Young's modulus to two times smaller values to show similar trends to the experimental data. The modes induced by excitation of the orifice fit the experimental results quite well for the length variation experiments, as seen in both figures. Furthermore, experimental results in the axial and radial direction seem quite similar when plotted against vessel length, with the radial modes seemingly having a slightly lower frequency.

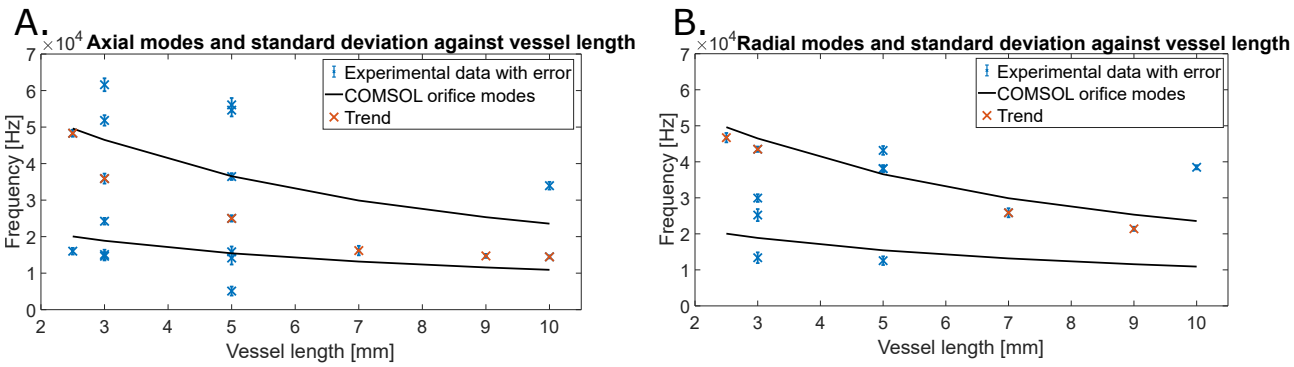

Figure 6.8: Plot of the axial (figure A) and radial (figure B) length variation results. Numerical and experimental data is shown in blue while trends following the numerical data are shown in red. For the numerical model we used a Young's modulus of 0.78 GPa for better comparison, 2 times smaller than we measured for the HTM140 V2

After this study, we used the same data to obtain the transfer function between the axial and radial sides with the goal of cross-checking the results. For the transfer function, we use the axial side as input and the radial side as output. This transfer function looks at the differences in attenuation between axial and radial modes but says nothing about the mode locations directly. Instead, it highlights the differences between the two directions. In figure 6.9, the colour plot of the mean for each vessel length against frequency and power can be seen. Darker areas represent areas with more radial power, while lighter areas generally have more axial power. Note that the colour bar is skewed as axial pulses generally have a larger signal-to-noise ratio. For an impression of the standard deviation and mean of the transfer function for one length, L = 5 mm, see appendix F.

In figure 6.9, we see a slight decrease in the frequency content of the first radial mode observed around 10 kHz, shown with the white dashed line. This indicates that the radial peaks of the first mode lie slightly lower than axial peaks of the same mode. This could be due to the larger attenuation in the radial direction, also observed when comparing the axial and radial directions in figure 6.8.

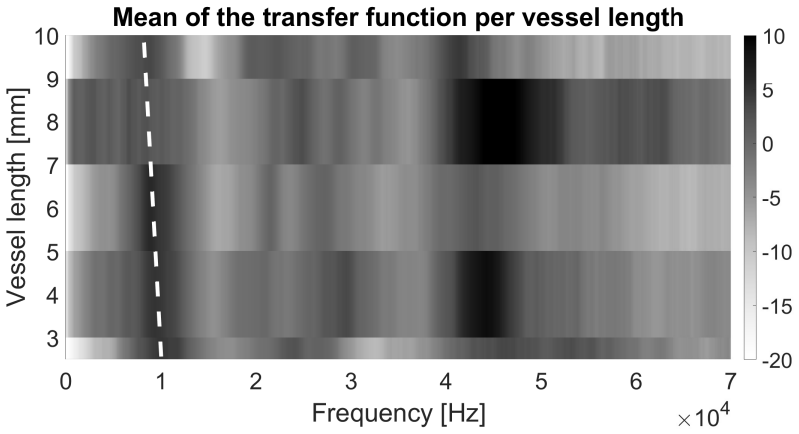

Figure 6.9: Mean of the transfer function for each vessel length against the power spectrum observed. The white dashed line shows a trend in the data

Aside from the transfer function, we also studied the decay time for each pulse to observe the impact of varying the vessel length on the decay time. This was done for both the axial and the radial directions. The results of this for type 2 and type 3 pulses can be seen in figures 6.10A and B. Once again, we see a significant difference in settling time between the two pulse types. Comparing the decay time for different vessel lengths, we observe no impact of the vessel length on the settling time. Furthermore, the standard deviation in the radial settling time seems to be slightly larger than the axial settling time. Finally, the settling time in the radial direction seems to be slightly shorter for type 3 pulses.

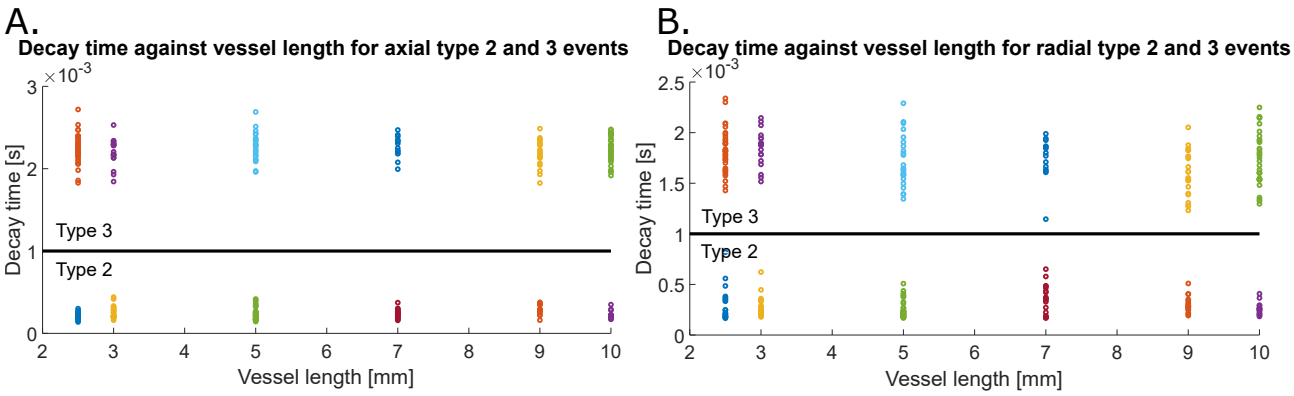

Figure 6.10: This figure shows the decay time of type 2 and type 3 pulses while measuring in the axial (figure A) and radial direction (B). The vessel length does not seem to have an influence on the settling time

6.6.2 Radius variation

After the length variation experiments, we looked into the influence of radius variation on the frequency spectrum. Similarly, we predicted the mode shapes for each inspected radius of the vessel. The results can be seen in figures 6.11A and B. We see how the first orifice mode fits the lower observed eigenmodes nicely with varying radii in the axial direction. The experimental values also fit reasonably well for the radial direction, despite the relatively limited amount of observed modes in this direction.

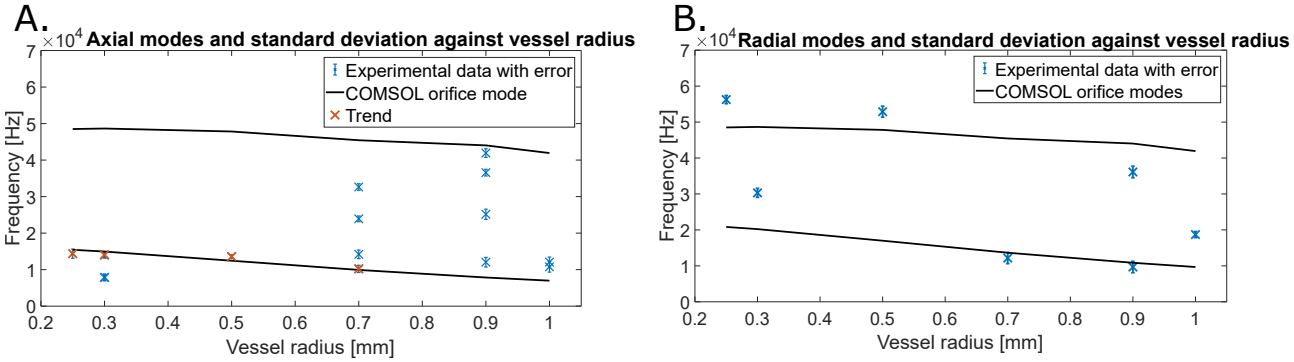

Figure 6.11: Plot of the axial (figure A) and radial (figure B) radius variation results. Numerical and experimental data is shown in blue while trends following the numerical data are shown in red. For the numerical model we used a Young's modulus of 0.78 GPa for better comparison, 2 times smaller than we measured for the HTM140 V2

Similar to the length variation for each different vessel radius, we took the mean over the transfer function between the axial and radial direction ($H = abs(\frac{radial}{axial})$). In figure 6.12, the colour plot of the vessel length against frequency and power can be seen. Again, darker areas represent areas with more radial power, while lighter areas generally have more axial power. Similar to the length variation, we see a slight decrease in the frequency content of the first radial mode observed around 10 kHz. Furthermore, there seems to be a trend of radial peaks between 30 to 50 kHz, especially visible when looking from a 3D perspective. This trend is visible in the raw data for the radial experimental results. These peaks, however, are slightly more spread out and filtered out in between steps 5 and 6 shown in figure 5.3.

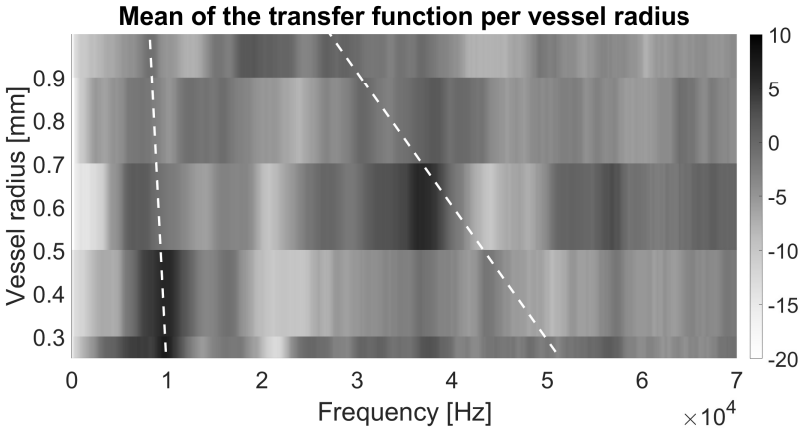

Figure 6.12: Mean of the transfer function for each vessel radius against the power spectrum observed. The white dashed lines show trends in the data. The higher frequency trend is more easily visible while inspecting in the plot in 3D

Due to the equation proposed by Dutta et al. [12], predicting the relationship between the settling time and the radius of xylem vessels, we checked the decay time for the radius variation

measurements. Once again, this time surprisingly considering the proposed formula, we observe no clear trend between the vessel radius and the decay time of type 2 and type 3 pulses. Furthermore, similar behaviour as seen in the previous section is observed with a difference in standard deviation and mean on the decay time between axial and radial pulses. The results of the decay time for type 2 and type 3 pulses can be seen in figure 6.13.

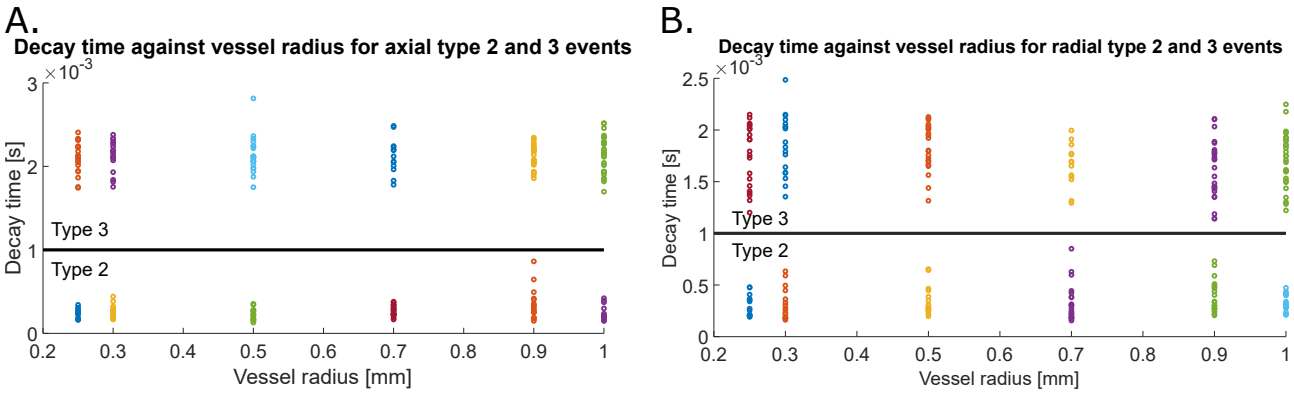

Figure 6.13: This figure shows the decay time of type 2 and type 3 pulses while measuring in the axial (figure A) and radial direction (B). The vessel radius does not seem to have an influence on the settling time

6.6.3 Filter paper pore radius

While trying to validate the by Dutta et al. [12] proposed formula for estimating the radius of a xylem vessel, we found the settling time to not vary too much for type 2 pulses. Furthermore, both the length and radius variation experiments show that neither pulse type changes significantly with geometry changes. When we do use equation 2.5 to estimate the radius of the vessel for type 2 pulses, we find a mean of 29.01 microns with a standard deviation of $\pm$ 20.84 microns. The distribution of the radii can be found in figure 6.14. This mean is remarkably close to the specified particle retention of the VWR 417 grade filter paper, which is specified to be 40 microns.

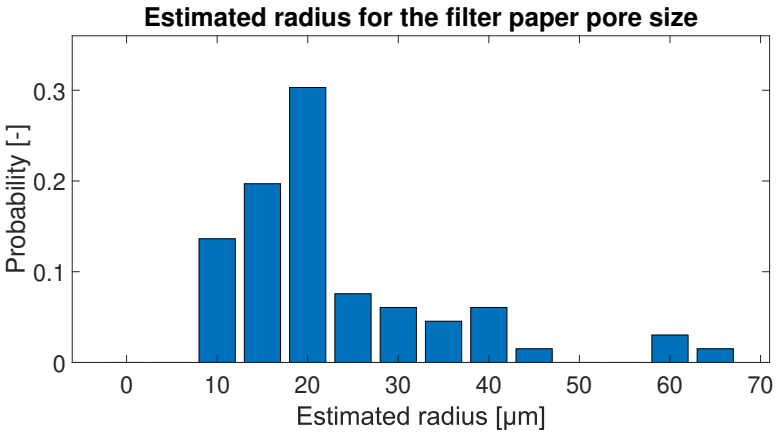

Figure 6.14: Estimated radius distribution calculated using the settling time of each pulse and equation 2.5. The particle retention of the filter paper is specified to be 40 microns, remarkably close to the mean value of our estimated pore radius

Chapter 7

Discussion

This chapter discusses the results in the same order as they were presented. We start with the evaporation studies in section 7.1, move on to the microscope studies in section 7.2 and study the waveforms along with the acoustic sources we observe in section 7.3. The numerical results are presented in section 7.4. We conclude the discussion with the results of the geometry variation in section 7.5.

7.1 Evaporation studies

During the study on the evaporation rate, much water initially evaporates rapidly from the surface of the structure and the wet filter paper, leading to many acoustic events. Pulses from the structure's surface likely do not enjoy the same attenuation as those inside the vessel or the filter paper. However, we observed their pulse-type to be of type 3, meaning we do not use them in the geometry variation experiments. After the water outside the vessel has evaporated, the events are more likely to originate inside the vessel. This would implicate that the pulses further on in the experiment have a more significant chance of originating from the vessels. Further studies might capitalise on this by only using acoustics after a certain weight has been attained. One downside of this method is that the vessel will have partly drained, changing the acoustics of the vessel.

7.2 Microscope studies

Using the microscope, we observed how water evaporation from the surface generates a small number of pulses. We found a match between the snapback of the water observed under the microscope and an acoustic emission on the microphone, shown in figure 6.1A. We observe that the resulting pulse carries type 3 pulse characteristics, inferring that drainage effects induce some slower type 3 acoustic emissions. The likely explanation for the lack of measured acoustic emissions from these events is their low power. In the case of figure 6.1A, the fluid front receded somewhat quicker than normal, which might explain why this pulse did trigger the microphone.

Aside from fluid front dynamics, in a few cases we observed bubbles in the vessels. Perhaps these bubbles appeared due to improper charging of the vessels, as observed by Shi et al. [15] in their artificial plant structure. When bubbles did appear, they did not embolise the vessel, indicating the water's tension was not high enough. In addition to this, we did not observe the fluid front recede from a seemingly random point due to nucleation of a bubble as observed by Ponomarenko et al. [11] in plants. Following Shi et al. [15], this might be due to the Young-Laplace pressure being too low inside of the filter paper. Using the equation proposed by Shi et

al. 2.1 we find a Young-Laplace pressure of 7.28 kPa for the filter paper, assuming the particle retention of 40.00 microns as the pore diameter, standard environmental conditions and using an optimal contact angle. This low pressure would lead to the fluid front not being trapped at the filter paper interface. Instead, the fluid front recedes, leading to a lack of pressure build-up. We also observe this in our vessels, even with filter paper clamped on both sides.

Following Wheeler et al. [20], a tension of about 1 MPa is necessary for cavitation to occur. Using the same formula, the pore diameter in the membrane should be lower than 0.28 μm to allow for these levels of tension on the liquid column. Several options for this have been shown in literature, including the nanoporous ceramic disk by Shi et al. [15] and the hydrogel and nanoporous AAO membrane used by Wang et al. [14].

7.3 Waveform analysis and acoustic sources

Using the pulses from the evaporation experiments, we could discern three types of waveforms based on their characteristics. However, the reality is most likely more complex. Without observing the source of the acoustic emissions due to their microscopic nature, further, more precise classification is impossible. Based on their settling time and amplitude, we discerned the waveforms. Type 1 acoustics most likely occur at a frequency much higher than we measure, indicating their source is more microscopic than the other types of events. These type 1 pulses should be further studied with a higher sampling rate microphone in follow up experiments to find out more about their origin. Their likely source is very fast dynamic events like bubble oscillation and Haines jumps on the smallest scale [25].

We recorded type 2 pulses in great numbers during drying of the filter paper, but also during the evaporation of water remnants in vessels and the evaporation of water from fluid-filled vessels. In the last case, these pulses occurred later in the experiment, where parts of the vessel had already drained. Therefore, one likely source of these pulses is drainage action in pores and imperfections in the filter paper and 3D printed material. Liquid bridge rupture and Haines jumps seem to fit the characteristics we observe in terms of settling time and frequency content. For Haines jumps, Moebius et al. [25] proposes time scales of 1 to 10 ms for 10-100 micron pore sizes, and 10-1000 kHz responses based on Scruby [46] and Lockner [47]. Similarly, for liquid bridge rupture, Michlmayr et al. [48] observed breakage times of 1 to 20 ms. A final observation is that these stronger type 2 emissions generally had a much more pronounced frequency content. In future studies, this bodes well for using cavitation-induced emissions, which generally have a lot of energy associated with them.

The type 3 events most likely originate from larger-scale events like macro fractures due to thermal expansion, as seen in figure 6.4A, and fluid-front displacements, as seen in figure 6.1B. Type 3 pulses were also recorded on the filter paper and in the vessel with water remnants, meaning more unknown sources exist. We observed a wide range of rise times for these type of pulses, again indicating the many different possible sources. This rise time might be used in future studies for further characterisation of the pulses. One possible source for the filter paper type 3 acoustics would be grain collision, as mentioned by Moebius et al. [25].

To conclude the topic of sources in our artificial plant structures, two of the lower frequency events also postulated by Vergeynst et al. [9], are likely to occur in our artificial structures: Haines jumps and macro-cracks. For our pulse types, these events fit in two different categories, which distinction might also be made in plants. Furthermore, in both type 2 and type 3 events, sometimes a beating of the pulse was observed after the main pulse. However, the time difference between these pulses was too significant for the second pulse to be a reflection travelling through the vessel. Perhaps this beating occurs due to fluid dynamics from one pore exciting dynamics in nearby pores.

Finally, in figure 6.2, one can see an exponential fit between the settling time and pulse

amplitude. This is likely an artefact of the method used for estimating the settling time. As the higher amplitude pulses have a steeper decline to the noise level, the estimated settling time is lower. Inspecting the settling time for some pulses by hand shows lower settling times for the lower amplitude pulses as the signal quickly falls below the noise level.

7.4 Numerical studies

The numerical studies shown in section 6.5 allowed for an initial prediction of the eigenmodes of the vessel. However, we made some simplifications for the model. For example, we chose to fix the boundaries of the two clamped side vessels instead of using a spring foundation of the 3D printed materials Young's modulus. The results we found were in line with expectations for most mode shapes except for a few modes in the radius variation simulations. During these simulations, we observed the radial modes to go up from 23 kHz at 250 microns radius to 27 kHz for 700 microns and back down to 25 kHz again for 1000 microns. This seems rather counter-intuitive. Furthermore, the axial breathing mode for this radius variation was also observed to remain constant with varying vessel radii around 57 kHz. These two results might indicate errors in the model or they might be caused by shifts in the bending inertia and rigidity with increasing radii.

7.5 Geometry variation - vessel length and radius

Interpretation of the impact of varying the geometry of the vessels is difficult due to a large amount of possible acoustic sources with different frequency contents. While attenuation of the vessel remains the same, one pulse might have a local minimum around an important frequency where the vessel has a specific eigenmode. The result would be a neutral frequency which we would not pick up in the analysis. One way to prevent this is by using a transducer to induce a sine sweep instead of using unknown acoustic sources.

Inspecting the histograms by hand showed that some significant modes were left out if they did not have one prominent peak but instead manifested as a multitude of smaller peaks near each other. In order to obtain better results, we could dial down the required prominence of the peaks. Doing so reveals many of these less prominent modes, yet it also takes away the attention from the more prominent modes. Despite the limited number of modes observed using our method, some trends seem visible. Finally, damping in the system shifts down the resonant frequencies to the peak frequencies we observe. Therefore, we can expect the resonant frequencies to lie slightly higher. Some quick calculations using the mean settling time of type 2 pulses to calculate the damping ratio (shown in section 2.4.2) shows that this increases the frequency content of these peaks by about 1.66 %, bringing the experimental results slightly closer to numerical results.

Finally, an inspection of the settling time of axial and radial pulses revealed no clear differences between the two. This would indicate that the by Dutta et al. [12] proposed axial and radial settling times are dictated by the origin of the acoustic pulse. As the origin for type 2 pulses, we observed how there might be a correlation between the pore size of the filter paper and the resulting settling time. A quick study using different household evaporative membranes proved indecisive as their pore sizes were too close together for a decisive result. Further studies with more extreme differences in pore sizes might show whether the seeming correlation between filter paper pore size and settling time was a coincidence.

Chapter 8

Conclusion

This thesis proposes a novel method for studying acoustic emissions in plants using artificial 3D printed structures. With the help of filter paper, we induced evaporation on a microfluidic vessel and inspected the resulting pulses in the time and frequency domain. Doing so, we replicated a multitude of acoustic emissions that likely also occur in plants. The main subject of interest in plants, air-seeding and cavitation events, was not replicated. However, using our newfound knowledge, the path to replication of these acoustic events now also lies open.

Using these artificial plant structures, we identified a multitude of evaporation and drainage induced sources of acoustic emissions. These sources include fluid front displacement, material expansion, water evaporation from surfaces, and water evaporation from porous membranes. Similar to plants, as shown in by Vergeynst et al. [9], we also observed multiple clusters of pulses in our artificial structure. We categorised resulting pulses into three types based on their settling time and amplitude. The first pulse-type we observed has dynamics too fast to capture with the used microphone. Sources for these pulses could include microscopic Haines jumps, bubble oscillation and bubble entrainment. The second type had a settling time below 1 ms and strong acoustic power. At the start of the experiment, we found the likely origin to be the evaporation of water from the filter paper. Further on in the experiment, they might be induced due to the evaporation of water from imperfections in the 3D printed material. Sources for this type of event will mainly be Haines jumps. The third pulse type consisted of slower events and likely constitutes many sources of pulses. Observed sources include thermal expansion of the 3D printed material and fluid-front dynamics. Many acoustic events in these experiments will have similar acoustics as we can observe in plants. One example would be how the heating of the artificial structure induces acoustic events as the solid structure expands. A similar event to this would be elastic shrinkage in plants due to drought stress, which was observed to induce acoustic emissions by Vergeynste et al. [9].

Using a newly proposed method in which we look for peak frequencies observable in multiple pulses, we observed a downwards shift of the axial eigenmodes with increasing vessel length and radius. When we compare the observed eigenmodes to the predicted modes using numerical simulation, we find these modes to be induced by the excitation of the orifice. This bodes well for the by Dutta et al. [12] proposed axial prediction of xylem vessel modes, equation 2.6. The large influence of the orifices also suggests that further studies are necessary on the influence of orifice excitation on the eigenmodes of xylem vessels. We also observed similar behaviour in the radial and axial direction for the vessels, indicating the axial modes should be visible in both directions in plants as well. Furthermore, we cross-checked the results with the transfer function between the axial and radial directions to confirm results from the new method. Finally, the by Dutta et al. proposed equation for the settling time, equation 2.5, predicted radii remarkably close to the particle retention of the filter paper for type 2 pulses.

These type 2 pulses likely originate from the filter paper, as shown by the multitude of pulses seen in figure 6.4B. Therefore, this equation might predict the source geometry, in this case the pore radius of the filter paper instead of the vessel radius. Further studies are necessary on this topic, however.

This thesis has improved our knowledge of acoustic emissions observed in plants and evaporation induced acoustics in a more general sense. Using our results, non-invasive monitoring of microfluidic devices becomes a possibility. Drainage of a microfluidic device would generate acoustic emissions detectable using a microphone which might be used to ensure continuity of fluid flow, perhaps in organs on a chip. The method we used could also be used in further studies by plant physiologists to cluster pulses, inspect their origin by separating specific parts of the plants and observing their drainage behaviour under a microscope. Furthermore, the prevalent influence of the orifice on the induced axial modes indicates its impact in plants might need to be considered in estimating the axial frequency response.

8.1 Recommendations

Many variables in the xylem vessel still have unknown impacts on the frequency response. Further studies on the impact of the Young's modulus, orifice diameter, fluid viscosity, and the xylem vessel thickness might paint a clear picture of their impact on the eigenfrequencies. Furthermore, we can also improve on the current experiment by pushing the printed geometry limitations to observe clearer relations. Printing longer vessels and smaller vessel diameters will clearly distinguish the frequencies we observe and bring our vessels closer to plants. Smaller diameter vessels should also shift the frequency spectrum upwards, which would lead to fewer problems with the current microphone, which quickly drops off below 10 kHz.

Instead of studying 3D printed plants, some research on the TU Delft has been done on printing real plant structures by Kunal Massania. Perhaps a collaboration with their department might allow for some degree of control on the parameters of these printed plants. Finally, future research could also use an additional microphone with a higher sampling rate to characterise the type 1 pulses and their fast dynamics. Perhaps these high frequencies contain useful information about the vessel structure. Similarly, adding a microphone with enough gain at lower frequencies could allow for better studies of type 3 pulses.

Aside from the other experiments, further studies are necessary on the main acoustic event we look for in plants: nucleation and cavitation. We used filter paper as our artificial leaf structure to induce a pressure drop over the vessel. This filter paper had a pore size close to 40 microns in diameter (its particle size retention). However, to induce the required large pressure drop on the vessel, a membrane with a much smaller pore size is necessary, as used by Shi et al. [15]. Perhaps acoustic events due to bubble nucleation can be observed using a similar ceramic nanoporous membrane clamped on the structure. The time it takes for this nucleation to occur, which will be very substantial, could be significantly decreased in a manner similar to Fernández et al. [49] by using a laser to add energy to the vessel. Another option would be to excite the vessel using an acoustic transducer. Aside from the ceramic membrane used by Shi et al., two other membranes are shown in the literature that can help induce cavitation. In their synthetic mangrove, Wang et al. [14] used hydrogel and an AAO membrane to replicate the leaf structure. Whatever membrane is used should be clamped tightly on the vessel structure to ensure no air gap exists.

To conclude, our recommendation for the most exciting follow-up study is as follows: Firstly, it should be checked whether bubble nucleation can be induced in the manner described above. If this is the case, using one of the three proposed membranes and a laser or acoustic transducer, this bubble nucleation and resulting acoustic emission and visual event should be studied. For this, a method similar to the method used in this thesis can be used. This one research could lead to advances and publications on the following topics:

- Bubble theory: Several studies have already been performed on the topic of bubble nucleation and subsequent growth (for example, by Doinikov et al. [41]). Understanding of their growth in microfluidic tubes is limited, however, with only one exciting paper found in the literature by Ilinskii et al. [42].
- Mode shapes of microfluidic 3D printed tubes: Knowing the mode shapes of microfluidic tubes might bring further applications like on-chip mass sensing in a way similar to Lee et al. [50]. The vessel might be excited with a cell inside, where the frequency shift could be used to estimate the mass/size of the cell. This process could easily be combined on a lab on a chip, where multiple processes are performed in series.
- Acoustic cavitation events and their origin in plant structures: By inducing cavitation through multiple methods, including air-seeding and pure cavitation, the origin of cavitation events in plant structures can be proven. The pit structures of plants might be replicated by creating nano-scale perforations to verify the hypothesis on the source of air-seeding proposed by Schenk et al. [19].
- Verification of the formulae proposed by Dutta et al. [12] and characterisation of the pulse shapes of cavitation induced pulses should also be further studied in this setup. The stronger acoustics will present clearer results than obtained during this thesis. Knowing the frequency domain signature of the air-seeding induced pulses will help recognising these events in plants, perhaps leading to a more accurate prediction of xylem vessel geometry.

Bibliography

[1] J. A. Milburn and R. Johnson, "The conduction of sap," *Planta*, vol. 69, no. 1, pp. 43–52, 1966.

[2] J. A. Milburn, "Cavitation studies on whole ricinus plants by acoustic detection," *Planta*, vol. 112, no. 4, pp. 333–342, 1973.

[3] M. T. Tyree, M. A. Dixon, E. L. Tyree, and R. Johnson, "Ultrasonic acoustic emissions from the sapwood of cedar and hemlock: an examination of three hypotheses regarding cavitations," *Plant Physiology*, vol. 75, no. 4, pp. 988–992, 1984.

[4] S. Rosner, A. Klein, R. Wimmer, and B. Karlsson, "Extraction of features from ultrasound acoustic emissions: a tool to assess the hydraulic vulnerability of norway spruce trunkwood?," *New Phytologist*, vol. 171, no. 1, pp. 105–116, 2006.

[5] C. R. Brodersen, A. J. McElrone, B. Choat, E. F. Lee, K. A. Shackel, and M. A. Matthews, "In vivo visualizations of drought-induced embolism spread in vitis vinifera," *Plant physiology*, vol. 161, no. 4, pp. 1820–1829, 2013.

[6] L. L. Vergeynst, M. Dierick, J. A. Bogaerts, V. Cnudde, and K. Steppe, "Cavitation: a blessing in disguise? new method to establish vulnerability curves and assess hydraulic capacitance of woody tissues," *Tree Physiology*, vol. 35, no. 4, pp. 400–409, 2015.

[7] L. L. Vergeynst, M. G. Sause, M. A. Hamstad, and K. Steppe, "Deciphering acoustic emission signals in drought stressed branches: the missing link between source and sensor," *Frontiers in plant science*, vol. 6, p. 494, 2015.

[8] L. De Roo, L. L. Vergeynst, N. J. De Baerdemaeker, and K. Steppe, "Acoustic emissions to measure drought-induced cavitation in plants," *Applied Sciences*, vol. 6, no. 3, p. 71, 2016.

[9] L. L. Vergeynst, M. G. Sause, N. J. De Baerdemaeker, L. De Roo, and K. Steppe, "Clustering reveals cavitation-related acoustic emission signals from dehydrating branches," *Tree physiology*, vol. 36, no. 6, pp. 786–796, 2016.

[10] D. Oletic, S. Rosner, M. Zovko, and V. Bilas, "Time-frequency features of grapevine's xylem acoustic emissions for detection of drought stress," *Computers and Electronics in Agriculture*, vol. 178, p. 105797, 2020.

[11] A. Ponomarenko, O. Vincent, A. Pietriga, H. Cochard, É. Badel, and P. Marmottant, "Ultrasonic emissions reveal individual cavitation bubbles in water-stressed wood," *Journal of the Royal Society Interface*, vol. 11, no. 99, p. 20140480, 2014.

[12] S. Dutta, E. Kaiser, P. Matamoros, P. Steeneken, and G. Verbiest, "Listening to ultrasound from plants reveals xylem vessel anatomy," 2021.

[13] P. G. Dixon, J. T. Muth, X. Xiao, M. Skylar-Scott, J. A. Lewis, and L. Gibson, "3d printed structures for modeling the young's modulus of bamboo parenchyma," *Acta biomaterialia*, vol. 68, pp. 90–98, 2018.

[14] Y. Wang, J. Lee, J. R. Werber, and M. Elimelech, "Capillary-driven desalination in a synthetic mangrove," *Science advances*, vol. 6, no. 8, p. eaax5253, 2020.

[15] W. Shi, R. M. Dalrymple, C. J. McKenny, D. S. Morrow, Z. T. Rashed, D. A. Surinach, and J. B. Boreyko, "Passive water ascent in a tall, scalable synthetic tree," *Scientific reports*, vol. 10, no. 1, pp. 1–9, 2020.

[16] M. D. Venturas, J. S. Sperry, and U. G. Hacke, "Plant xylem hydraulics: what we understand, current research, and future challenges," *Journal of Integrative Plant Biology*, vol. 59, no. 6, pp. 356–389, 2017.

[17] M. M. Wróblewska, "The progressive and ancestral traits of the secondary xylem within magnolia clad-the early diverging lineage of flowering plants," *Acta Societatis Botanicorum Poloniae*, vol. 84, no. 1, 2015.

[18] G. Jackson and J. Grace, "Field measurements of xylem cavitation: are acoustic emissions useful?," *Journal of Experimental Botany*, vol. 47, no. 11, pp. 1643–1650, 1996.

[19] H. J. Schenk, K. Steppe, and S. Jansen, "Nanobubbles: a new paradigm for air-seeding in xylem," *Trends in plant science*, vol. 20, no. 4, pp. 199–205, 2015.

[20] T. D. Wheeler and A. D. Stroock, "The transpiration of water at negative pressures in a synthetic tree," *Nature*, vol. 455, no. 7210, pp. 208–212, 2008.

[21] Y.-X. Guan, Z.-R. Xu, J. Dai, and Z.-L. Fang, "The use of a micropump based on capillary and evaporation effects in a microfluidic flow injection chemiluminescence system," *Talanta*, vol. 68, no. 4, pp. 1384–1389, 2006.

[22] C. S. Effenhauser, H. Harttig, and P. Krämer, "An evaporation-based disposable micropump concept for continuous monitoring applications," *Biomedical microdevices*, vol. 4, no. 1, pp. 27–32, 2002.

[23] W. Shi, J. R. Vieitez, A. S. Berrier, M. W. Roseveare, D. A. Surinach, B. R. Srijanto, C. P. Collier, and J. B. Boreyko, "Self-stabilizing transpiration in synthetic leaves," *ACS applied materials & interfaces*, vol. 11, no. 14, pp. 13768–13776, 2019.

[24] I. Khait, R. Sharon, R. Perelman, A. Boonman, Y. Yovel, and L. Hadany, "Plants emit remotely detectable ultrasounds that can reveal plant stress," *bioRxiv*, p. 507590, 2019.

[25] F. Moebius, D. Canone, and D. Or, "Characteristics of acoustic emissions induced by fluid front displacement in porous media," *Water Resources Research*, vol. 48, no. 11, 2012.

[26] Z. Sun and J. C. Santamarina, "Haines jumps: Pore scale mechanisms," *Physical review E*, vol. 100, no. 2, p. 023115, 2019.

[27] D. d. O. França Júnior, P. M. V. Ribeiro, and L. J. Pedroso, "Simplified expressions for dynamic behavior of cylindrical shells uncoupled and coupled with liquids," *Latin American Journal of Solids and Structures*, vol. 16, no. 6, 2019.

[28] M. A. Temiz, J. Tournadre, I. L. Arteaga, and A. Hirschberg, "Modelling vibro-acoustic coupling in flexible micro-perforated plates by a patch-impedance approach," *Applied Acoustics*, vol. 125, pp. 80–90, 2017.

[29] L. J. Gibson, "The hierarchical structure and mechanics of plant materials," *Journal of the royal society interface*, vol. 9, no. 76, pp. 2749–2766, 2012.

[30] M. J. Männel, L. Selzer, R. Bernhardt, and J. Thiele, "Optimizing process parameters in commercial micro-stereolithography for forming emulsions and polymer microparticles in nonplanar microfluidic devices," *Advanced Materials Technologies*, vol. 4, no. 1, p. 1800408, 2019.

[31] A. K. Au, W. Huynh, L. F. Horowitz, and A. Folch, "3d-printed microfluidics," *Angewandte Chemie International Edition*, vol. 55, no. 12, pp. 3862–3881, 2016.

[32] R. K. Lade Jr, E. J. Hippchen, C. W. Macosko, and L. F. Francis, "Dynamics of capillary-driven flow in 3d printed open microchannels," *Langmuir*, vol. 33, no. 12, pp. 2949–2964, 2017.

[33] N. P. Macdonald, J. M. Cabot, P. Smejkal, R. M. Guijt, B. Paull, and M. C. Breadmore, "Comparing microfluidic performance of three-dimensional (3d) printing platforms," *Analytical chemistry*, vol. 89, no. 7, pp. 3858–3866, 2017.

[34] G. Weisgrab, A. Ovsianikov, and P. F. Costa, "Functional 3d printing for microfluidic chips," *Advanced Materials Technologies*, vol. 4, no. 10, p. 1900275, 2019.

[35] A. I. Shallan, P. Smejkal, M. Corban, R. M. Guijt, and M. C. Breadmore, "Cost-effective three-dimensional printing of visibly transparent microchips within minutes," *Analytical chemistry*, vol. 86, no. 6, pp. 3124–3130, 2014.

[36] M. Monzón, Z. Ortega, A. Hernández, R. Paz, and F. Ortega, "Anisotropy of photopolymer parts made by digital light processing," *Materials*, vol. 10, no. 1, p. 64, 2017.

[37] A. K. Au, W. Lee, and A. Folch, "Mail-order microfluidics: evaluation of stereolithography for the production of microfluidic devices," *Lab on a Chip*, vol. 14, no. 7, pp. 1294–1301, 2014.

[38] R. B. Wicker, A. V. Ranade, F. Medina, and J. A. Palmer, "Embedded micro-channel fabrication using line-scan stereolithography," *Assembly Automation*, 2005.

[39] H. Gong, B. P. Bickham, A. T. Woolley, and G. P. Nordin, "Custom 3d printer and resin for 18 μm$\times$ 20 μm microfluidic flow channels," *Lab on a Chip*, vol. 17, no. 17, pp. 2899–2909, 2017.

[40] H. Gong, M. Beauchamp, S. Perry, A. T. Woolley, and G. P. Nordin, "Optical approach to resin formulation for 3d printed microfluidics," *RSC advances*, vol. 5, no. 129, pp. 106621–106632, 2015.

[41] A. A. Doinikov, B. Dollet, and P. Marmottant, "Model for the growth and the oscillation of a cavitation bubble in a spherical liquid-filled cavity enclosed in an elastic medium," *Physical Review E*, vol. 97, no. 1, p. 013108, 2018.

[42] Y. A. Ilinskii, E. A. Zabolotskaya, T. A. Hay, and M. F. Hamilton, "Models of cylindrical bubble pulsation," *The Journal of the Acoustical Society of America*, vol. 132, no. 3, pp. 1346–1357, 2012.

[43] N. J. De Baerdemaeker, M. Stock, J. Van den Bulcke, B. De Baets, L. Van Hoorebeke, and K. Steppe, "X-ray microtomography and linear discriminant analysis enable detection of embolism-related acoustic emissions," *Plant methods*, vol. 15, no. 1, pp. 1–18, 2019.

[44] V. Srikanth, E. C. Subbarao, D. K. Agrawal, C.-Y. Huang, R. Roy, and G. V. Rao, "Thermal expansion anisotropy and acoustic emission of nazr2p3o12 family ceramics," *Journal of the American Ceramic Society*, vol. 74, no. 2, pp. 365–368, 1991.

[45] E. Aznarte, C. Ayranci, and A. Qureshi, "Digital light processing (dlp): Anisotropic tensile considerations," in *2017 International Solid Freeform Fabrication Symposium*, University of Texas at Austin, 2017.

[46] C. B. Scruby, "An introduction to acoustic emission," *Journal of Physics E: Scientific Instruments*, vol. 20, no. 8, p. 946, 1987.

[47] D. Lockner, "The role of acoustic emission in the study of rock fracture," in *International Journal of Rock Mechanics and Mining Sciences & Geomechanics Abstracts*, vol. 30, pp. 883–899, Elsevier, 1993.

[48] G. Michlmayr, D. Cohen, and D. Or, "Sources and characteristics of acoustic emissions from mechanically stressed geologic granular media—a review," *Earth-Science Reviews*, vol. 112, no. 3-4, pp. 97–114, 2012.

[49] E. Fernández, R. J. Fernández, and G. M. Bilmes, "Natural and laser-induced cavitation in corn stems: On the mechanisms of acoustic emissions," *arXiv preprint arXiv:1205.3398*, 2012.

[50] D. Lee, S. Kaub, and J. Lee, "Pulled microcapillary tube resonators for high precision microdroplet size measurements," in *2017 IEEE 30th International Conference on Micro Electro Mechanical Systems (MEMS)*, pp. 1146–1149, IEEE, 2017.

Appendix A

Orifice geometry

The geometry of the orifices that divide the different vessel elements, as described in section 4.1, is shown in this section in figure A.1. The orifices have a thickness of 300 microns, a pore diameter of 375 microns and an outer diameter of 500 microns. Furthermore, they contain a large fillet to improve the print quality. While varying the radius of the vessels, the pore size stays the same. This means that the orifice turns into a relatively flexible membrane between the vessels for larger radii.

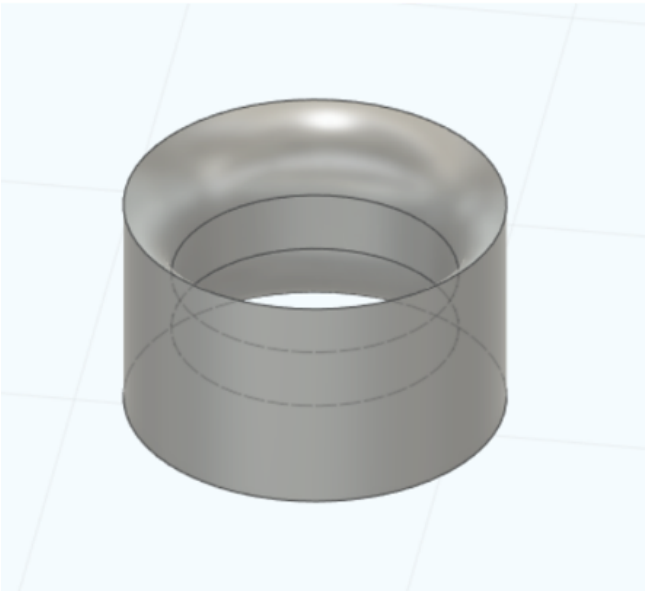

Figure A.1: Geometry of the orifices that divide vessels in the artificial plant structures. With radius variation the pore size remains the same while the orifice outer radius becomes larger

Appendix B

Picture of the full experimental setup

The full setup used for the experiments can be found in this appendix, while the schematic setup can be found in section 5.1. The following components can be seen in the figure:

1. An incandescent light bulb to heat the box - Philips low voltage incandescent lamp 40W
2. The dehumidifier bag to decrease the box humidity - Pingi car dehumidifier
3. The microscope - 2.0M Pixels digital microscope USB
4. A microphone - Batsound M500
5. The temperature and humidity sensor - Lascar EL-USB-2 Temperature and Humidity data logger
6. Extra lighting to provide light from under the sample to increase visibility inside of the vessel

Figure B.1: Setup used for the measurements (excluding the lid and using 1 microphone). All components mentioned above are visible

Appendix C

Environmental conditions in the setup

As described in section 5.2 the temperature and humidity can be seen to increase and decrease, respectively. This was done using the light bulb and dehumidifying pouch to keep the environment more consistent during measurements and not wait for days on experiments when the weather is humid. A typical experiment has the light bulb on for 25 minutes, increasing the temperature in the box. Usually, a temperature between 30 and 40 degrees Celsius is attained depending on the room temperature. After that, the light bulb is switched off not to damage any equipment. During this phase, most evaporation from the filter paper occurs, leading to many acoustic events. The filter paper has dried after about 90 to 120 minutes. The dehumidifying pouch decreases the humidity inside the box during the entire experiment. The effect of the increasing temperature decreasing humidity in the air is also quite visible, as when the temperature decreases again, humidity goes up too.

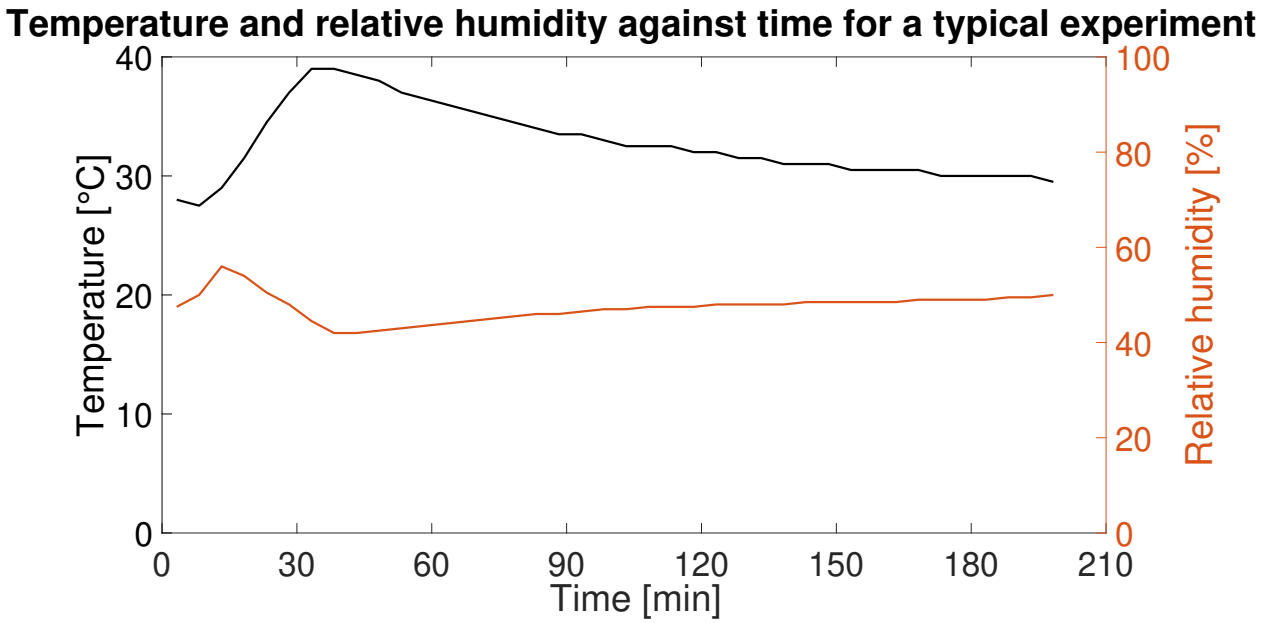

Figure C.1: Example of the increase and decrease of temperature and humidity during a measurement, temperature is shown in black and humidity in red

Appendix D

Tensile modulus of the printed material

This appendix describes how the tensile modulus of the printer material, in the print direction, was measured as mentioned in section 5.1. In order to determine the tensile modulus of the to be used HTM140 V2 material, ASTM D638 test strips with halved dimensions were used due to printer size constraints. Four samples were printed and tensile loaded using the Zwick/Roell Z005 Uniaxial tensile loading machine until they broke. The force applied and the elongation were measured by the machine. Using the known geometry of the strip, these were converted to the stress and elongation of the sample. The resulting linear regime of the data can be seen in figure D.1. Using the linear regime, we found the Young's modulus to be 1.56 GPa for the HTM140 V2 material.

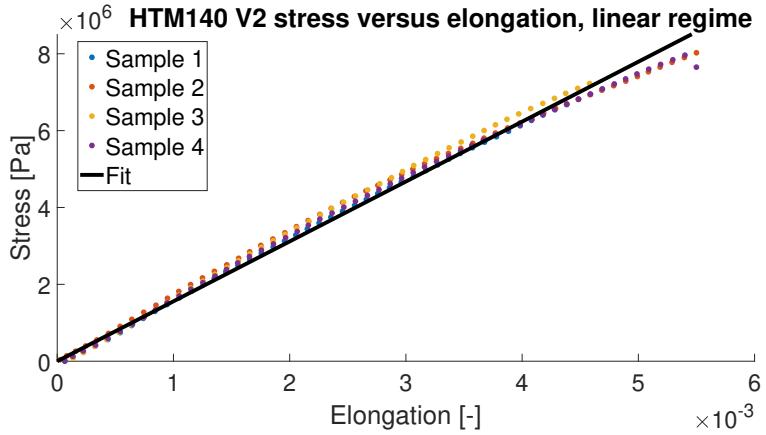

Figure D.1: The linear regime of the tensile loading with added fit used to calculate the tensile modulus

Similarly, the Young's modulus of the 3DM Tough Clear material was obtained with a smaller test strip. For this material, the dimensions of the ASTM D638 test strip dimensions were divided by 4. The tensile test resulted in a tensile modulus of 1.84 GPa for this material.

Appendix E

Frequency domain of the pulse types

In this appendix, the different observed waveforms are shown as described in section 6.3. Figure E.1 shows the 3 types of observed waveforms in frequency domain.

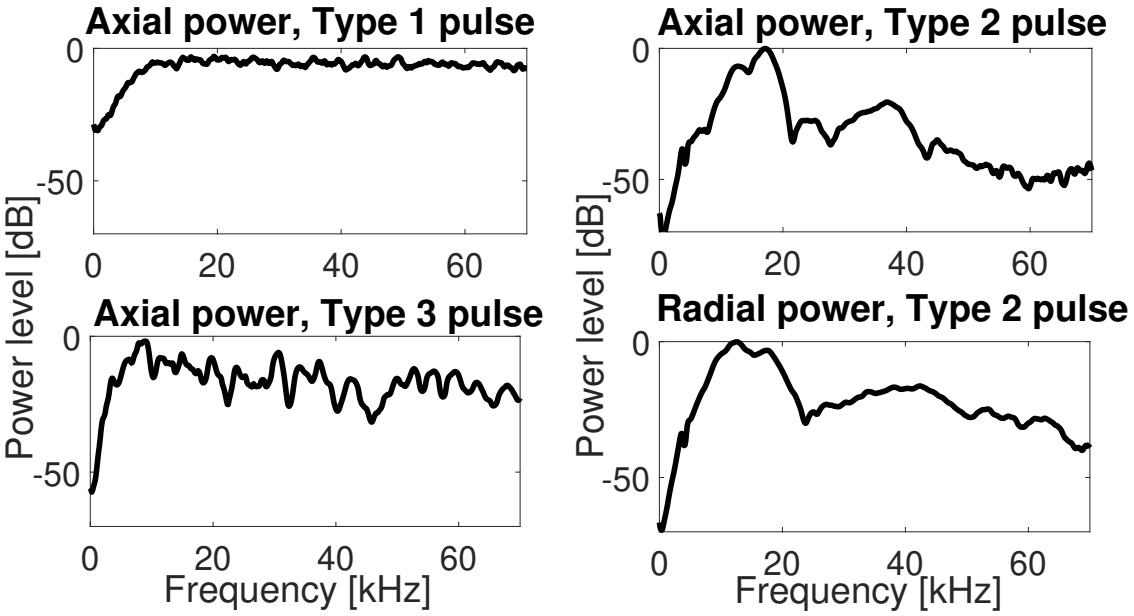

Figure E.1: Example of the frequency domain of a type 1, 2 and 3 pulse in axial direction and the same type 2 pulse in radial direction. Note that the pulses are normalised and the axial power for figure A is lower as the peak lies above 70 kHz

Appendix F

Standard deviation of the transfer function

In this appendix, an example is given of the mean and standard deviation of the transfer function between the axial and radial direction. The standard deviation between about 5 to 35 kHz is fairly low (maximum of 10 dB).

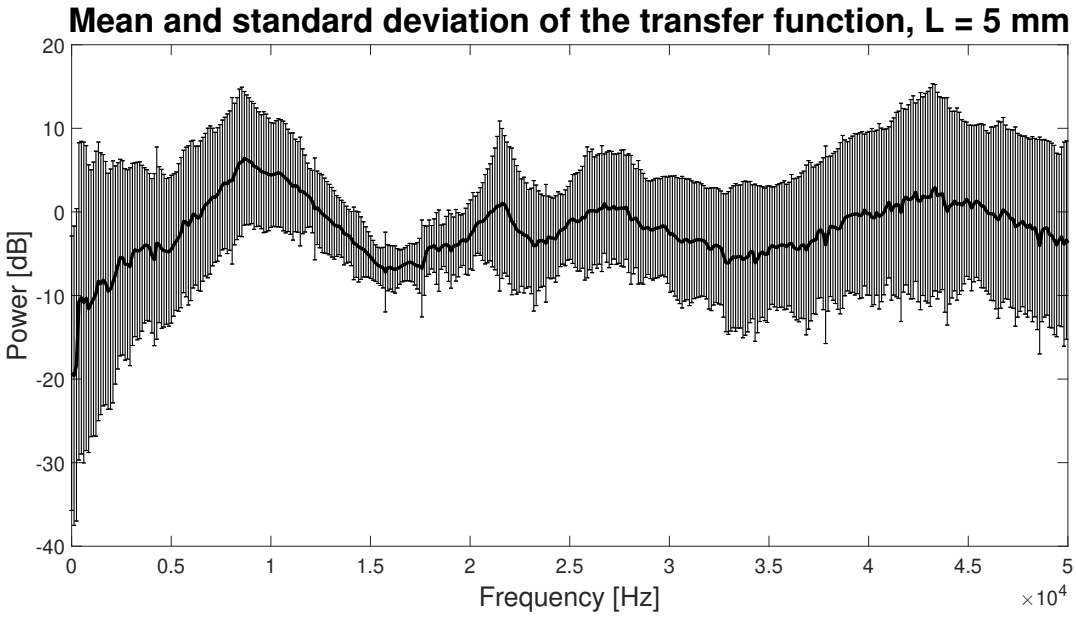

Figure F.1: Example of the mean and standard deviation on the transfer function between the axial and radial direction for L = 5 mm

INTERFACE

rsif.royalsocietypublishing.org

Research

Article submitted to journal

Subject Areas:
microfluidics

Keywords:
microfluidics, acoustics, 3D printing, evaporation, ultrasound

Author for correspondence:
Satadal Dutta
e-mail: S.Dutta-1@tudelft.nl

THE ROYAL SOCIETY
PUBLISHING

Evaporation induced acoustic emissions in microfluidic vessels

T.J. Bieling [1], S. Dutta [1], G.J. Verbiest [1]

[1] Department of Precision and Microsystems Engineering, Faculty of 3ME, TU Delft, Mekelweg 2, 2628CD Delft, the Netherlands

Evaporation can induce acoustic emissions in microfluidic devices. The origin of these emissions and their damping remains elusive. This article studies acoustic emissions from 3D printed microfluidic tubes mimicking xylem vessels in plants. We show the time and frequency domain signature of these emissions. From these signatures, we identify three types of acoustic pulses. While the source of the first type remains elusive, the second type originates from our evaporative membrane and the third from slower events like microcracking. By varying the vessel's geometry, we observe that its frequency shifts down with increasing vessel radius and length for the second pulse type. We confirmed this behaviour using numerical simulations of the vessel. These findings provide new insights into evaporation induced acoustic emissions from microfluidic devices and, due to their similar morphology, xylem vessels in plants.

1. Introduction

In 1966 the plant physiologists Milburn and Johnson [1] showed how drought stress in plants induces bubbles and accompanying ultrasonic emissions [2]. The bubbles subsequently embolise the vessel [3] leading to a decrease in the plants capacity to supply water to the leaves [4], which was studied extensively [5–9]. Recently, the focus has started to shift more to the characteristics of the induced emissions [3, 9–12]. Following this trend, Dutta et al. [13] observed pulses related to the vessel geometry and material properties.

We study the relationship between pulse characteristics and vessel geometry to observe similar relations in microfluidic vessels mimicking xylem vessels. These relations would allow us to estimate xylem vessel properties. In general, these relations could also be used for monitoring tubes in microfluidics and pipe flow engineering [14]. In microfluidics, acoustics could allow for the detection of fluid front displacement [15], and possibly even microdroplet size measurements similar to Lee et al. [16]. In pipe flow engineering, acoustics allow for detecting fatigue cracks [17] and leaks [18] before they cause significant problems.

Options exist in the literature to mimic natural plant structures using microfluidic devices. Wheeler et al. [19] for example, created planar channels in pHEMA sheets. Using stereolithography, we can devise more complex 3D geometries albeit at lower resolution [20] compared to soft lithography. We will use this method, which has recently enjoyed interest from fields like healthcare [21], organs on a chip [22, 23] and labs on a chip [24, 25]. In order to further mimic the xylem vessels, we separated our vessel into three vessel elements using orifices, replicating the perforation plates between xylem vessels.

We induce acoustics through evaporation from a porous membrane [26]. As water evaporates, the microporous membrane traps water using its surface tension up to a tension dictated by the Young-Laplace equation A 2. Sudden relaxation of this tension releases acoustic emissions. As our membrane, we use filter paper inspired by Guan et al. [27] and Effenhauser et al., [28] who used it for pumping purposes. We placed the filter paper and vessel in a box of elevated temperature and reduced humidity to speed up evaporation.

© The Authors. Published by the Royal Society under the terms of the Creative Commons Attribution License http://creativecommons.org/licenses/by/4.0/, which permits unrestricted use, provided the original author and source are credited.

In this box we recorded acoustic emissions from the 3D printed water-filled vessels and filter paper. We identified sources of acoustic emissions using different experimental conditions. From this, we recognised three types of waveforms, of which we linked one to the vessel geometry using the frequency spectrum of the pulse. This linking was in agreement with numerical simulations indicating that mechanical resonances of the orifice determine the observed frequencies. The method used can also prove helpful in studying other sources of acoustic emissions and their relation to the geometry they are confined in.

2. Methods

The methodology starts with the fabrication in section (a). Then we show the setup in which we recorded ultrasound emissions in section (b) and the data processing in section (c).

(a) Fabrication

We chose the EnvisionTEC Micro Plus Hi-Res as our 3D printer for its high resolution and low surface roughness. This digital light processing (DLP) printer uses a projector with pixels of 30 microns to harden resin on specified locations in layers of 50 microns high. Its limited resolution constrains the size of the printed vessels. Too small vessel dimensions cause the resin to clog the channel as the liquid resin remains stuck while printing [29]. Experimentation with vessel dimensions and clogging found vessels with a radius of 150 microns to be printable.

The structures were modelled in Fusion360, sliced using the Perfactory RP software and printed. The 3D printed structure consists of a tube of which the outer two sides are clamped by a solid structure around it, as seen in figure 1A. Orifices separate the vessel into individual vessel elements. We utilised two different types of resin for the experiments. The first is HTM140 V2, a translucent resin with a Young's modulus around 1.56 GPa, determined in a tensile test found in the supplementary document. The second material is the more transparent 3DM Tough Clear with a Young's modulus of 1.84 GPa. We used this 3DM resin while studying under the microscope but not during the geometry variation as it was more likely to clog than the HTM140 V2 resin.

After printing, we rinsed the structures in an ultrasonic bath (Bandelin Sonorex RK31) and dried them. Using a pump with 2 bars of operating pressure, the vessels were cleaned and, in some cases, unclogged. Finally, we hardened the structures in a Dentalfarm Photopol Light Curing unit using UV cold light for 3 minutes and UV spots for 3 minutes. Lastly, we hydrated the vessels in water until necessary for the experiments.

(b) Setup

We used an anechoic box to study the acoustic emissions. An incandescent 40W Philips light bulb increased the temperature in this box, while a Pingi dehumidifier decreased the humidity, thereby enhancing drought. In this setup, we observed events inside the vessel under a 2.0M Pixels Digital Microscope USB. We measured acoustic emissions along and perpendicular to the vessel with a Batsound M500 microphone, placed around 1 to 5 millimetres from the vessel. The measurement directions and a schematic of the setup are demonstrated in figure 1B, along with a picture of the setup in figure 1C. The microphone was triggered if an acoustic emission exceeded -30 dB in the axial or -40 dB power in the radial direction. This power level ensures that triggered pulses have sufficient acoustic power for further use. We chose a lower power level for the radial direction as radial pulses generally carried less energy due to larger attenuation. Triggering saves data 0.2 seconds before and up to 2 seconds after the trigger with a sampling frequency of 500 kHz.

An experiment starts by making sure the vessel is fully hydrated, wet filter paper (VWR Grade 417) is placed at one open end of the vessel, and the entire structure is placed under the microscope and near the microphone. A Lascar EL-USB-2 logs the temperature and humidity data during the measurements. The box is closed while we switch on the light bulb and start the measurements with the microphone. Twenty-five minutes into the experiment, we switched off the light bulb as the temperature approached 40 degrees Celsius. During initial measurements, we stopped the experiment when no pulses had been recorded for 1 hour, which sometimes took up to half a day. However, we chose to stop the geometry variation experiments after 2 hours as most pulses have occurred by then.

(c) Data processing

After the experiments, we process the recorded pulses. The offset in time between pulses in the radial and axial measurements was determined. If the pulses in both directions occurred within 0.1 seconds of each other, we read the generated .wav file using MATLAB and saved the maximum pulse amplitude and settling time from the time domain. The settling time was calculated using a logarithmic fit on the envelope of the pulse. In order to obtain the transfer function between the axial and radial direction, we used the `tfestimate` function in MATLAB with a Hanning window. We use the axial side as the input and the radial side as output for this function. When calculating the power spectrum, we used the `pwelch` function with the same settings. See the supplementary document for a more in-depth explanation of the data processing, functions used, and why we chose specific settings.

3. Results

As a first step, we inspected the evaporation rate during an experiment by measuring the structure's mass on a weighing scale. Simultaneously, we used a microscope to estimate the mass inside the vessel and added the mass of the dry structure to this to compare to the measured mass.

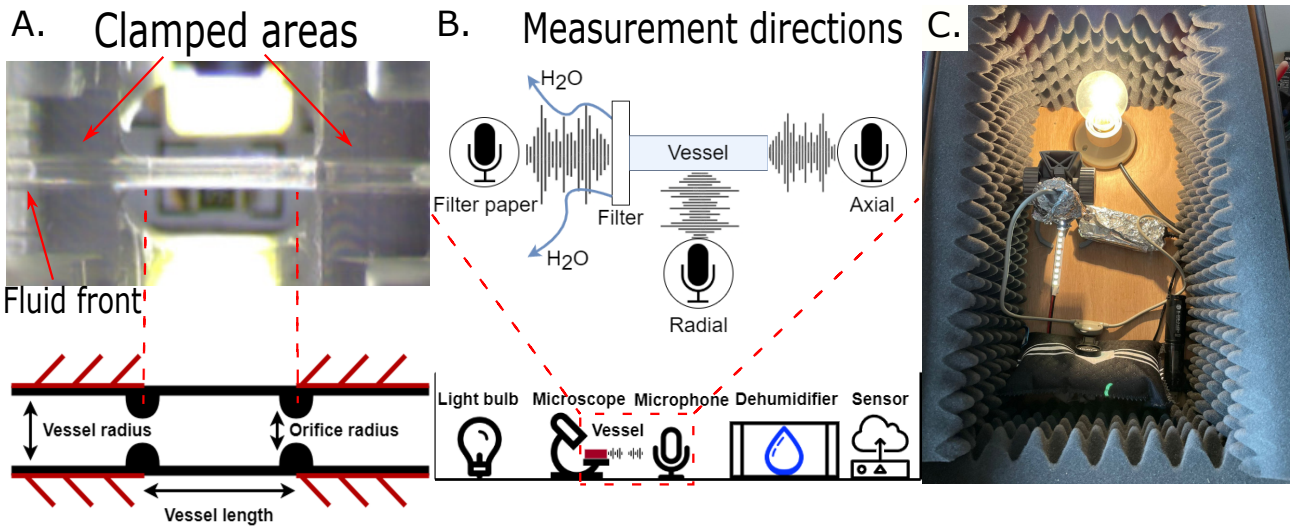

Figure 1: This figure summarises the methods. Figure A shows a schematic of the vessel structure and the vessel as seen under the microscope. Furthermore, in this figure, we show the location of the orifices and fluid front. In figure B, we see a schematic of the setup and the measurement directions, along with the location of the filter paper. Finally, in figure C a picture of the setup is shown

Finally, we also listened for acoustic emissions during these measurements. The results are summarised in figure 2.

In the first 90 minutes, we hear many emissions as the measured mass rapidly decreases while the mass of water in the vessel decreases slowly. This means evaporation from the surface and the filter paper will be the likely source of these acoustic emissions. After this first part, denoted by the black line in figure 2, the measured mass and the mass of the water in the vessel slowly decrease while many emissions still occur for about an hour. These emissions are more likely to originate from inside the vessel. After about 4 hours, most acoustic events have happened while the fluid front slowly recedes for about 6 hours until it fully embolises the vessel.

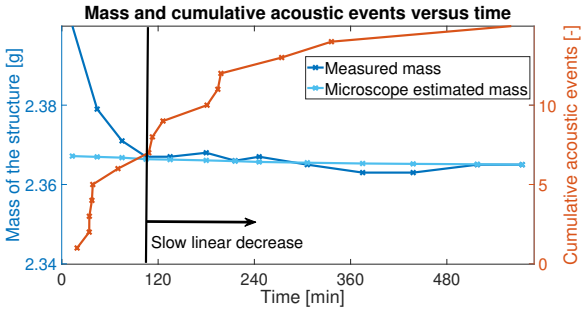

Figure 2: Evaporation rate of mass in the vessel and the cumulative acoustic events we measured. After the black line, most of the mass outside the vessel has evaporated as the mass slowly decreases, yet emissions still occur. The acoustics consist of axial pulses

The simultaneous optical and acoustic measurements showed drainage effects and accompanying acoustics. Drainage of the vessel occurred as follows: the fluid front recedes from the microphone side to the filter paper until the orifice traps it temporarily. Here it gathers enough tension to continue draining and then fully drains the vessel after passing the next orifice. We rarely observed bubbles. When they did appear, the fluid front subsequently entrained them. Perhaps those bubbles that did appear might be similar to Shi et al. [30] due to improper charging of the vessels. In one case, we found an optical event synchronised with an acoustic emission, shown in appendix B figure 8. Here the fluid front reaches an orifice inducing the pulse seen below the pictures of the vessel.

(a) Waveforms

Subsequently, we started looking into signal characteristics by simultaneously listening with microphones in the axial and radial directions. We observed three pulse types separable by their settling time and maximum pulse amplitude. These three pulse types are shown in figures 3A, B, and C. In figure 3D, this distinction between types can be seen with the formation of clusters. We left out type 1 events as their settling time is an order of magnitude smaller. The first pulse type, shown in figure 3A along with its settling time in red, has dynamics too fast to capture with the Batsound M500 microphone (250+ kHz), a low pulse amplitude and a very fast settling time of about 50 microseconds. Due to these fast dynamics, the frequency spectrum is featureless in the inspected range.

The second pulse type, shown in figure 3B, has the highest amplitude on average, a settling time around one millisecond and easily discernible peaks between 5 to 70 kHz. Peaks with the highest amplitude lie between 10 to 20 kHz, while higher frequency peaks are also visible up to 60 kHz (see appendix B, figures 9B and 9D). Finally, the third pulse-type had a longer settling time and medium pulse amplitude, as seen in figure 3C. Their frequency content

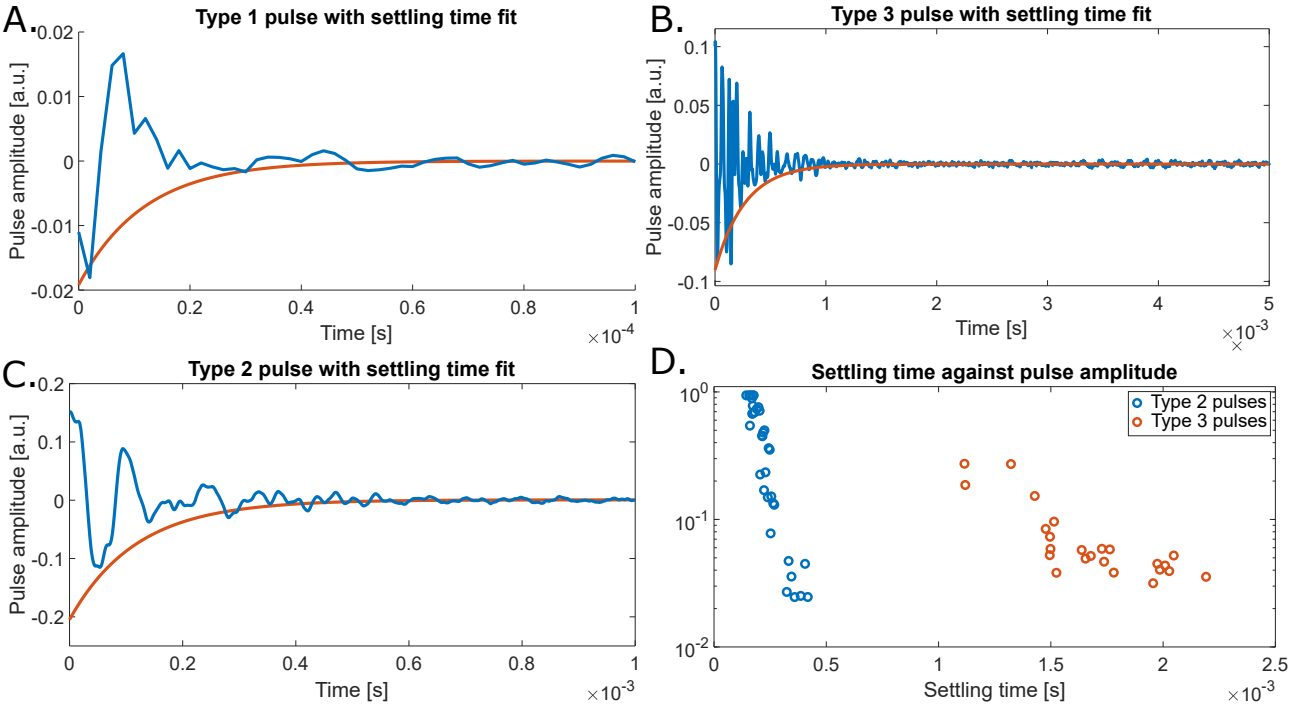

Figure 3: Figures A to C show an example of all three pulse types with their logarithmic fit, which we used to estimate the settling time. Figure D shows the settling time versus amplitude (logarithmic) for the type 2 and type 3 axial pulses. Type 1 pulses are not shown due to their very sharp settling time. They would be located in the bottom left of the figure

contains a lot of small peaks, which can be seen in appendix B, figure 9C.

(b) Acoustic sources

Background measurements showed a Welch's averaged noise level of -110 dB. After noting this, we studied different sources of acoustic emissions and their relation to the pulse types. The four most important sources are summarised in figure 4.

In the first experiment, shown in figure 4A, we studied a dry vessel without filter paper. The resulting pulses were generally of type 3 with a longer settling time and a slow rise time. Sources are likely due to the expansion of the 3D printed material. Emissions could be induced by microcracking of the material, something observed in ceramics by Srikanth et al. [31].

The second experiment on evaporation from filter paper, shown in figure 4B, had many acoustic events occurring. Most of the events occurred within 30 minutes, and nearly all were of type 2. Their frequency response is rich in peaks but shows barely any correlation between pulses. These acoustics can be explained mainly by Haines jumps, where the fluid inside the paper snaps back from the throat of one pore inside the filter paper to the next [15].

For the third experiment, shown in figure 4C, we measured on a drained vessel with water remnants inside. These remnants created only a few pulses, mainly of type 2, with very different dynamics. Sources might include snapback of water and evaporation of water from tiny pores on the surface of the 3D printed material.

Finally, we measured on a vessel without filter paper and without the light bulb heating the environment. This experiment, depicted in figure 4D, shows that type 1 events originate inside the vessel. Furthermore, several type 2 and type 3 events are observable. Sources of the observed events could include snap-off processes, bubble induced acoustics but also liquid bridge rupture [26], Haines jumps [15] or snap-off processes in the drained part of the vessel.

(c) Geometry variation - length and radius

In the last sets of experiments, we varied one geometrical parameter per experiment to observe its effect on the power spectrum of type 2 pulses. We used type 2 pulses for their significant acoustic power and clear attenuation compared to the other two pulse types. Using type 2 pulses means a lot of acoustics will have originated from the filter paper, as seen in the huge count of pulses of this type in figure 4B. We chose the following radii for the radius variation experiments: 0.25, 0.3, 0.5, 0.7, 0.9 and 1 mm (note that the pore diameter of the orifices did not change). For the length variation, we chose vessel lengths of: 2.5, 3, 5, 7, 9 and 10 mm.

Since the input dynamics of pulses show little correlation, the resulting frequency spectrum leads to a significant standard deviation when we take the mean over all the pulses of one geometry. Therefore, we devised a new method to find general peaks visible in multiple pulses of one geometry. A flowchart of the method is depicted in figure 5.

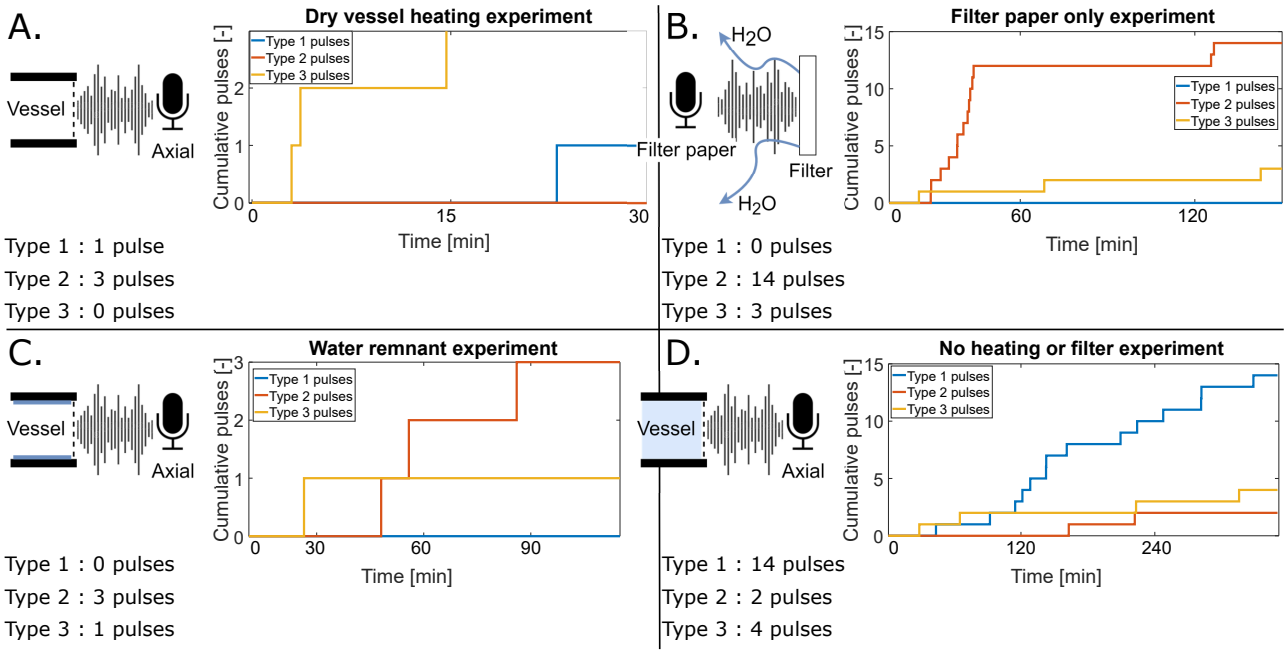

Figure 4: The four performed experiments on sources of acoustic emissions: heating a dry vessel, the wet filter paper, remnants of water in the vessel and the vessel without heating or filter paper. For all experiments, we used a sample with a length of 5 mm and a radius of 0.25 mm

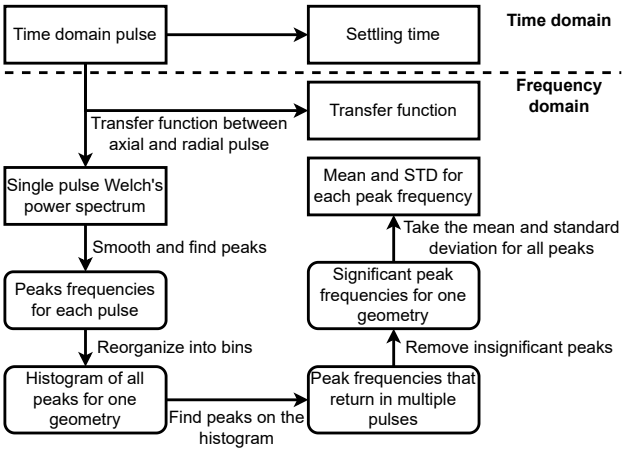

Figure 5: Flowchart of the methodology used starting with the time domain pulse. For an overview of three important functions we used see the supplementary document

Having obtained the Welch's power spectrum for every pulse, we smooth the power spectrum. Subsequently, we use the MATLAB `findpeaks` function on the smoothed spectrum with a minimum prominence of 5 to find only the significant peaks. We convert the resulting peaks for all pulses into bins to create a histogram for the given geometry. Subsequently, we find the local maxima on this histogram and filter out less significant peaks. This gives us peaks that occur in multiple pulses and thus have a high probability of being related to an event in the vessel. Using these peak frequencies, we take all single found peaks within 3 kHz for the studied geometry to calculate the mean and standard deviation. The 3 kHz was chosen based on results obtained from numerical simulation, as will be explained below. The extracted mean peak frequencies are what we denote as eigenmodes; their frequencies are plotted in figure 6.

To gain insight into the origin of the mean peak frequencies, we used COMSOL Multiphysics to simulate the eigenmodes of the structure for the previously presented geometry variations. The numerical model uses both the Solid Mechanics and Pressure Acoustics physics, which we coupled using the Acoustic-Structure boundary. We use the eigenfrequency solver between 1 to 70 kHz to find the relevant modes. Further details of the simulation are described in the supplementary document.

The main findings from these studies for both directions were that increasing the vessel's length or radius resulted in a decrease in frequency. Furthermore, we observed how the orifices play an essential role in dictating the resulting eigenfrequencies of the vessel. These numerical results are plotted along with the experimental results in figure 6.

We also used COMSOL to study the impact of our printing accuracy. In a test print, we observed a deviation of about six % from the modelled geometry, taking some extra margin deviations in the geometry of 10 % were simulated. The maximum observed deviation occurred with length variation, where a deviation of up to 3 kHz could occur for mode 2. We used this value as the area within which we look for the calculation of the mean and standard deviation of the modes, as explained above. Especially for the radius variation experiments, the impact of deviations will be quite low. For more information on the sensitivity, see the supplementary document.

After obtaining all the geometry variation results, they

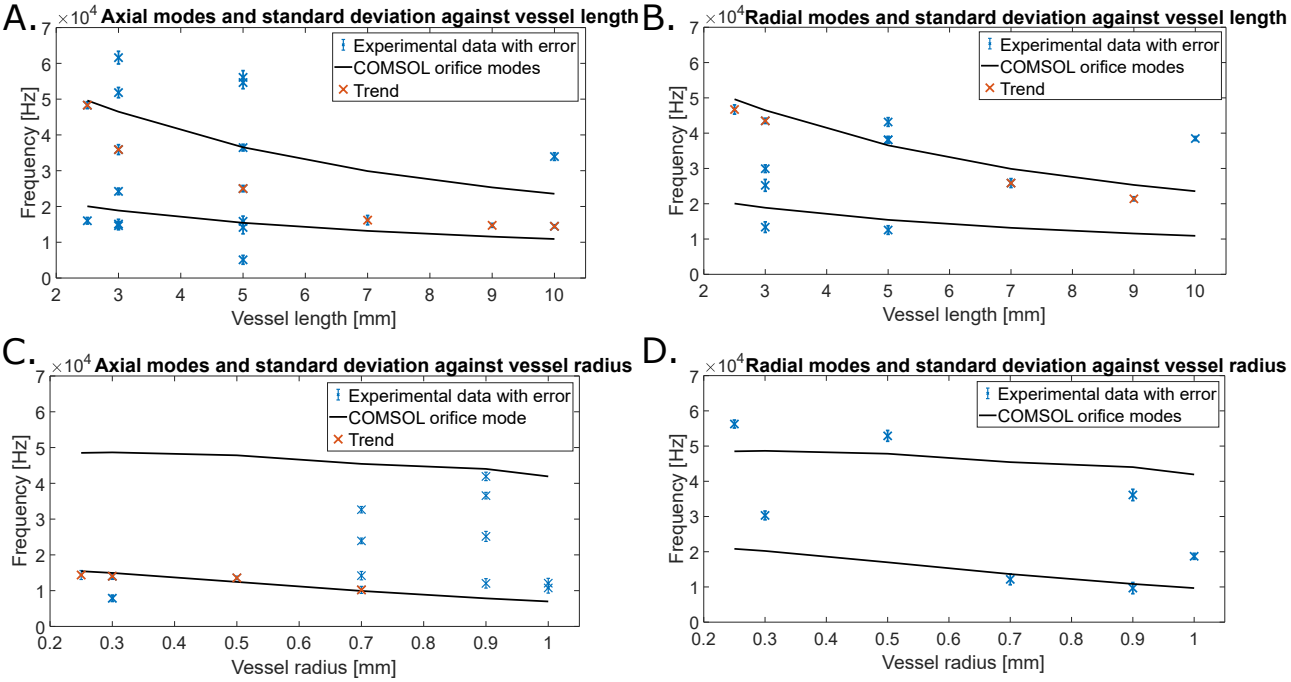

Figure 6: Plots of the geometry variation results. Shown are numerical and experimental data. For the numerical simulation, we used a Young's modulus of 0.78 GPa to show its similarity to the experimental results. In red, we marked trends that follow orifice modes with geometry variation

were plotted together with the numerical results. Since we modelled the Young's modulus in COMSOL as an isotropic material while, in reality, DLP printed structures are highly anisotropic [32], we can expect some margin of error. We scaled the Young's modulus to two times smaller values to show similar trends to the experimental data. The experimental and numerical results can be seen in figure 6. All found modes are plotted, showing the significant difference in the number of peaks found between experiments. Furthermore, in red clear trends in the data are shown that are similar to the experimental results.

The modes induced by excitation of the orifice fit the experimental results reasonably well for the length variation experiments, as seen in figures 6A and 6B. Furthermore, experimental results in the axial and radial direction seem quite similar when plotted against vessel length, with the radial modes seemingly having a slightly lower frequency.

In the axial direction, shown in figure 6C, we see how the first orifice mode fits the lower observed eigenmodes nicely with varying radii. The experimental values fit reasonably well for the radial direction, as seen in figure 6D. This experiment, however, does have a rather limited amount of observed modes.

Finally, we calculated the transfer function between the axial and radial pulses to cross-check our observed eigenmodes. Doing so tells us something about trends between the axial and radial directions. The transfer function against length and radius can be seen in figures 7A and 7B respectively. The length variation plots show a shift downwards in radial power compared to axial power from 10 to 8 kHz with increasing length (shown in the white dashed line). This trend is also visible while comparing the results from figures 6A and 6B, as we see the radial modes to lie slightly lower.

Something similar seems to be the case for radius variation starting at 11 kHz for a radius of 0.25 mm to 8 kHz for a radius of 1 mm. Furthermore, an interesting observation is the trend of radial peaks decreasing from around 50 to 30 kHz. This trend is visible in the raw data; however, it is filtered out by the mean peak height for the chosen modes. These results and their implications will be further discussed in the next section.

Finally, we investigated the settling time of the pulses. We observed no change with varying vessel radii, which might be explained by their origin lying in the filter paper. When we take the mean and standard deviation for type 2 pulses of the reference geometry, we get a mean of 0.24 $\pm$ 0.08 ms. Using equation A 1 the resulting mean radius for these type 2 events is 31.58 microns, while the particle retention of the filter paper is known to be 40.00 microns.

4. Discussion

(a) Waveforms

We discerned three types of waveforms from the acoustic signatures. However, the reality is most likely more complex. For example, a wide range of rise times is visible in type 3 events, hinting at many sources. We can, however, infer some things using the experiments we performed.

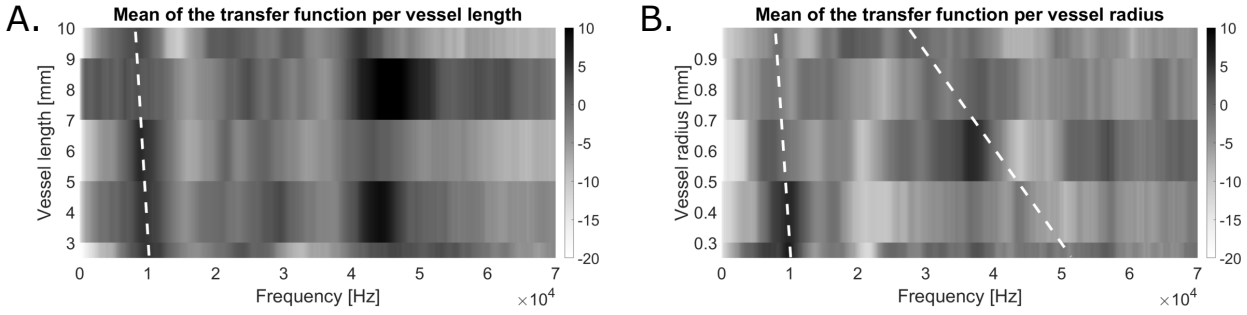

Figure 7: Mean transfer function between axial pulses as input and radial pulses as output against vessel length and radius. We use this to cross-check the geometry variation results. In white dashed lines, we show the trends we can observe

Firstly, the majority of type 2 pulses seems to occur in the first 30 minutes of the filter paper drying. Furthermore, some type 2 pulses occurred while water remnants evaporated from the vessel. This might also be the case in the experiment without filter paper and without heating of the structure, where the drained part of the vessel might excite pulses. The source of early type 3 events is likely from thermal expansion of the 3D printed material. Finally, we observed how a significant amount of pulses are correlated to the orifice modes seen in COMSOL. Their exact source remains elusive, however. In these cases, one likely origin is the relaxation of surface tension in either the filter paper pores or imperfections in the 3D printed material. These pulses then excite the orifices leading to the modes we observe.

The source of type 1 events lies in the vessel (figure 4D) and, due to their high-frequency dynamics, these are most likely related to fast dynamics like bubble oscillation [26]. Type 3 events likely constitute much more diverse sources, such as microcracks shown by experiment A, figure 4. Another type 3 event originated from the fluid-front hitting the orifice as shown in appendix B, figure 8.

(b) Acoustic sources

The source of the majority of acoustic emissions in our structure becomes clear from figures 2 and 4B: evaporation of water from the filter paper. Perhaps some of the later pulses originate from inside the vessel, albeit from the fluid (figure 4D) or water remnants in the empty part of the vessel (figure 4C).

Cavitation, as observed in plants, is unlikely to occur in our vessels. In none of the experiments, the fluid front receded from a seemingly random point due to nucleation of a bubble, as observed by Ponomarenko et al. [3]. When bubbles did appear, they did not embolise the vessel, indicating the tension on the water was not high enough to cause cavitation. This was checked by following Shi et al. [30] and calculating the Young-Laplace pressure (shown in appendix B equation A 2) in the filter paper. Using this equation, we find a Young-Laplace pressure of the filter paper of 7.28 kPa, assuming the particle retention of 40.00 microns as the pore diameter, standard environmental conditions and using an optimal contact angle.

Following Wheeler et al. [19] a tension of about 1 MPa is necessary for cavitation to occur, meaning the pore diameter in the membrane should be lower than 280 nm using the same formula. Further studies could use this to induce and study cavitation effects and its attenuation by artificial vessels. Several membranes can be found in the literature that fit the small pore size requirement. The first membrane that could be used is the nanoporous ceramic disk by Shi et al. [30]. Furthermore, Wang et al. show two different membranes that could be used: nanoporous AAO membranes and hydrogel [33].

(c) Geometry variation - length and radius

Interpretation of the impact of varying the parameters for the tubes is difficult due to a large amount of possible acoustic sources with different frequency content. While attenuation of the vessel remains the same, one pulse might have a local minimum around an important frequency where the vessel has a specific eigenmode. The result would be a neutral frequency which we would not pick up in the analysis. One way to prevent this is by using a transducer to induce a sine sweep instead of using unknown acoustic sources.

Inspecting the histograms by hand showed that some significant modes were left out if they did not have one prominent peak but instead manifested as a multitude of smaller peaks near each other. In order to obtain better results, we could dial down the prominence of the peaks. Doing so reveals many of these less prominent modes, which takes the attention away from the more prominent modes. Despite the limited number of modes observed using our method, some trends seem visible. Finally, damping in the system shifts down the resonant frequencies to the peak frequencies we observe. Therefore, we can expect the resonant frequencies to lie slightly higher, increasing the frequency by about 1.66 %, bringing the experimental results slightly closer to numerical results.

5. Conclusions

This paper proposes a novel concept for studying acoustic emissions in plants using artificial 3D printed structures. Using filter paper, we induced evaporation on a microfluidic

vessel and inspected the resulting pulses in time and frequency domain. Identified sources of acoustic emissions include fluid front displacement, material expansion, evaporation of water from surfaces and evaporation of water from porous membranes. We categorised resulting pulses into three types based on their settling time and amplitude.

Using a newly proposed method in which we look for peak frequencies observable in multiple pulses, we observed a downwards shift of the eigenmodes with increasing vessel length and radius. When we compare the observed eigenmodes to the predicted modes using numerical simulation, we find the these modes to be induced by the excitation of the orifice. Finally, we cross-checked the results with the transfer function between the axial and radial directions to confirm results from the new method.

This article brings us to a deeper understanding of evaporation induced acoustics in microfluidic vessels and their subsequent attenuation by the vessel. Similar studies could lead to advancements in identifying different types of plant emissions by plant physiologists. By characterising pulses, specific pulses might be coupled to adverse events allowing for monitoring of the plant. In microfluidics, acoustic emissions might allow for non-invasive monitoring of the continuity of fluid flow in devices, as draining of the vessel would induce acoustic emissions. This might be useful in monitoring organs on a chip. Finally, this study also highlights the influence of orifice modes in pipes and their impact on the frequency response.

A. Formulas

The following formula relates the settling time to the estimated radius of the vessel [13]. In this equation η_l represents the xylem sap viscosity, τ_{axial} the damping time of the envelope of the measured signal and ρ_l the density of the fluid.

$$R = \sqrt{\frac{4\eta_l \tau_{axial}}{\rho_l}} \tag{A 1}$$

The formula below is the Young-Laplace pressure. It predicts the capillary pressure difference between the water and air due to surface tension of the water [30]. In this equation γ is given as the surface tension, θ the contact angle of the pore and the liquid and r_{pore} the pore radius of the evaporative structure.

$$P_L = \frac{2\gamma\cos(\theta)}{r_{pore}} \tag{A 2}$$

B. Figures

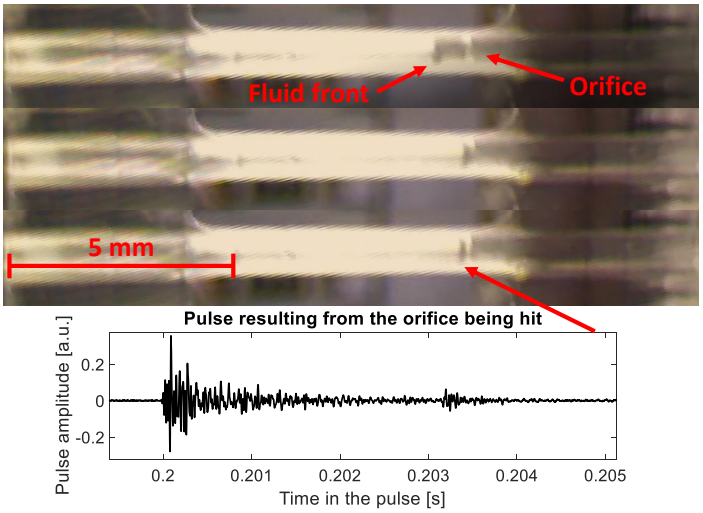

Figure 8: Example of a synchronous pulse inducing a type 3 axial event as the fluid front hits the orifice. In the first picture, the fluid front approaches, it reaches the orifice in the second picture and induces an acoustic emission in the third picture

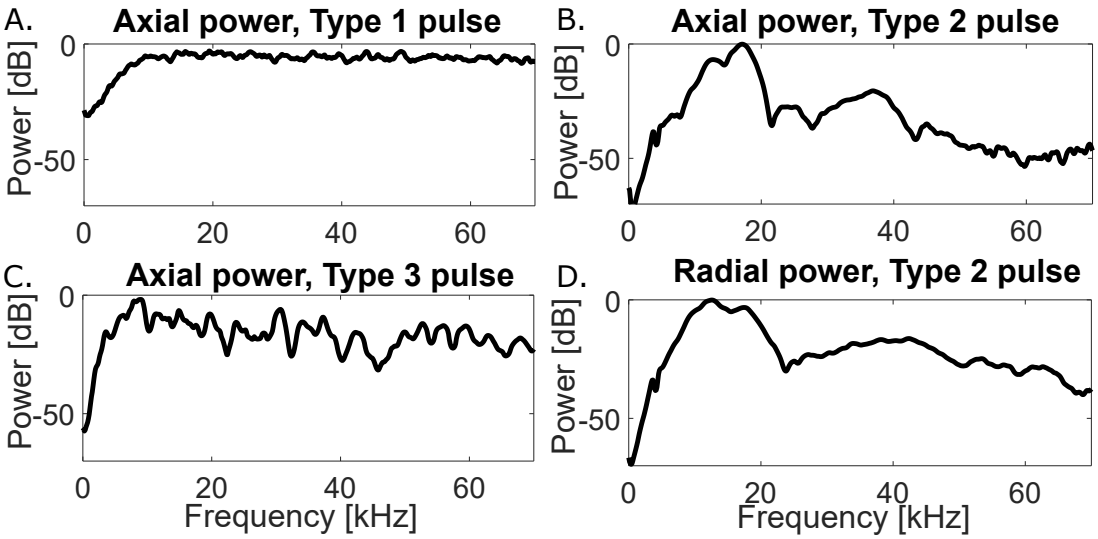

Figure 9: Example of the frequency domain of a type 1, 2 and 3 pulse in axial direction and the same type 2 pulse in radial direction. Note that the pulses are normalised and the axial power for figure A is lower as the peak lies above 70 kHz

Data Accessibility. Used data and further explanations on the project can be found in the supplementary.

Authors' Contributions. S.Dutta and G.Verbiest conceived the idea, provided the necessary equipment and supervised the work. T.Bieling conceived the experiments and conducted the 3D printing, measurements and writing.

Competing Interests. The authors declare no competing interests.

Funding. The research was funded as part of the 4TU "Plantenna" research programme.

Acknowledgements. This work has been carried out under the "Plantenna" research programme, a collaboration among the members (technical universities) of the 4TU federation in the Netherlands. The authors would like to thank Patrick van Holst, Bradley But and Gideon Emmaneel for technical support during fabrication and inspection of the artificial structures and help with operating the equipment.

References

[1] J. A. Milburn and R. Johnson, "The conduction of sap", Planta **69**, 43–52 (1966).

[2] M. T. Tyree, M. A. Dixon, E. L. Tyree, and R. Johnson, "Ultrasonic acoustic emissions from the sapwood of cedar and hemlock: an examination of three hypotheses regarding cavitations", Plant Physiology **75**, 988–992 (1984).

[3] A. Ponomarenko, O. Vincent, A. Pietriga, H. Cochard, É. Badel, and P. Marmottant, "Ultrasonic emissions reveal individual cavitation bubbles in water-stressed wood", Journal of the Royal Society Interface **11**, 20140480 (2014).

[4] M. D. Venturas, J. S. Sperry, and U. G. Hacke, "Plant xylem hydraulics: what we understand, current research, and future challenges", Journal of Integrative Plant Biology **59**, 356–389 (2017).

[5] J. A. Milburn, "Cavitation studies on whole Ricinus plants by acoustic detection", Planta **112**, 333–342 (1973).

[6] G. Jackson and J. Grace, "Field measurements of xylem cavitation: are acoustic emissions useful?", Journal of Experimental Botany **47**, 1643–1650 (1996).

[7] S. Rosner, A. Klein, R. Wimmer, and B. Karlsson, "Extraction of features from ultrasound acoustic emissions: a tool to assess the hydraulic vulnerability of Norway spruce trunkwood?", New Phytologist **171**, 105–116 (2006).

[8] H. J. Schenk, K. Steppe, and S. Jansen, "Nanobubbles: a new paradigm for air-seeding in xylem", Trends in plant science **20**, 199–205 (2015).

[9] I. Khait, R. Sharon, R. Perelman, A. Boonman, Y. Yovel, and L. Hadany, "Plants emit remotely detectable ultrasounds that can reveal plant stress", bioRxiv, 507590 (2019).

[10] L. L. Vergeynst, M. G. Sause, M. A. Hamstad, and K. Steppe, "Deciphering acoustic emission signals in drought stressed branches: the missing link between source and sensor", Frontiers in plant science **6**, 494 (2015).

[11] L. L. Vergeynst, M. G. Sause, N. J. De Baerdemaeker, L. De Roo, and K. Steppe, "Clustering reveals cavitation-related acoustic emission signals from dehydrating branches", Tree physiology **36**, 786–796 (2016).

[12] D. Oletic, S. Rosner, M. Zovko, and V. Bilas, "Time-frequency features of grapevine's xylem acoustic emissions for detection of drought stress", Computers and Electronics in Agriculture **178**, 105797 (2020).

[13] S. Dutta, E. Kaiser, P. Matamoros, P. Steeneken, and G. Verbiest, "Listening to ultrasound from plants reveals xylem vessel anatomy", (2021).

[14]S. Wöckel, U. Steinmann, and H. Arndt, "Low frequency guided wave transmission in water pipe systems", Procedia engineering **120**, 1257–1260 (2015).
[15]Z. Sun and J. C. Santamarina, "Haines jumps: Pore scale mechanisms", Physical review E **100**, 023115 (2019).
[16]D. Lee, S. Kaub, and J. Lee, "Pulled microcapillary tube resonators for high precision microdroplet size measurements", in 2017 IEEE 30th International Conference on Micro Electro Mechanical Systems (MEMS) (IEEE, 2017), pages 1146–1149.
[17]M. S. Khan and R. Patil, "Acoustic characterization of pvc sewer pipes for crack detection using frequency domain analysis", in 2018 IEEE International Smart Cities Conference (ISC2) (IEEE, 2018), pages 1–5.
[18]S. Li, Y. Song, and G. Zhou, "Leak detection of water distribution pipeline subject to failure of socket joint based on acoustic emission and pattern recognition", Measurement **115**, 39–44 (2018).
[19]T. D. Wheeler and A. D. Stroock, "The transpiration of water at negative pressures in a synthetic tree", Nature **455**, 208–212 (2008).
[20]A. K. Au, W. Lee, and A. Folch, "Mail-order microfluidics: evaluation of stereolithography for the production of microfluidic devices", Lab on a Chip **14**, 1294–1301 (2014).
[21]A. C. Daly, P. Pitacco, J. Nulty, G. M. Cunniffe, and D. J. Kelly, "3D printed microchannel networks to direct vascularisation during endochondral bone repair", Biomaterials **162**, 34–46 (2018).
[22]R. Zhang and N. B. Larsen, "Stereolithographic hydrogel printing of 3D culture chips with biofunctionalized complex 3D perfusion networks", Lab on a Chip **17**, 4273–4282 (2017).
[23]Y. He, Y. Wu, J.-z. Fu, Q. Gao, and J.-j. Qiu, "Developments of 3D printing microfluidics and applications in chemistry and biology: a review", Electroanalysis **28**, 1658–1678 (2016).
[24]R. Amin, S. Knowlton, A. Hart, B. Yenilmez, F. Ghaderinezhad, S. Katebifar, M. Messina, A. Khademhosseini, and S. Tasoglu, "3D-printed microfluidic devices", Biofabrication **8**, 022001 (2016).
[25]G. Weisgrab, A. Ovsianikov, and P. F. Costa, "Functional 3D printing for microfluidic chips", Advanced Materials Technologies **4**, 1900275 (2019).
[26]F. Moebius, D. Canone, and D. Or, "Characteristics of acoustic emissions induced by fluid front displacement in porous media", Water Resources Research **48** (2012).
[27]Y.-X. Guan, Z.-R. Xu, J. Dai, and Z.-L. Fang, "The use of a micropump based on capillary and evaporation effects in a microfluidic flow injection chemiluminescence system", Talanta **68**, 1384–1389 (2006).
[28]C. S. Effenhauser, H. Harttig, and P. Krämer, "An evaporation-based disposable micropump concept for continuous monitoring applications", Biomedical microdevices **4**, 27–32 (2002).
[29]M. J. Männel, L. Selzer, R. Bernhardt, and J. Thiele, "Optimizing Process Parameters in Commercial Micro-Stereolithography for Forming Emulsions and Polymer Microparticles in Nonplanar Microfluidic Devices", Advanced Materials Technologies **4**, 1800408 (2019).
[30]W. Shi, R. M. Dalrymple, C. J. McKenny, D. S. Morrow, Z. T. Rashed, D. A. Surinach, and J. B. Boreyko, "Passive water ascent in a tall, scalable synthetic tree", Scientific reports **10**, 1–9 (2020).
[31]V. Srikanth, E. C. Subbarao, D. K. Agrawal, C.-Y. Huang, R. Roy, and G. V. Rao, "Thermal expansion anisotropy and acoustic emission of NaZr2P3O12 family ceramics", Journal of the American Ceramic Society **74**, 365–368 (1991).
[32]E. Aznarte, C. Ayranci, and A. Qureshi, "Digital light processing (DLP): Anisotropic tensile considerations", in 2017 International Solid Freeform Fabrication Symposium (University of Texas at Austin, 2017).
[33]Y. Wang, J. Lee, J. R. Werber, and M. Elimelech, "Capillary-driven desalination in a synthetic mangrove", Science advances **6**, eaax5253 (2020).

C. Supplementary information

(a) Tensile modulus

This section describes how the tensile modulus of the printer material, in the print direction, was measured. In order to determine the tensile modulus of the to be used HTM140 V2 material ASTM D638 test strips with halved dimensions were used due to printer size constraints. We printed four samples and tensile loaded them using the Zwick/Roell Z005 Uniaxial tensile loading machine until they broke. The force applied and the elongation was measured by the machine. Using the known geometry of the strip, we converted force to the stress in the sample. The resulting linear regime of the test can be seen in figure 10. Using this regime, we found the Young's modulus to be 1.56 GPa for the HTM140 V2 material.

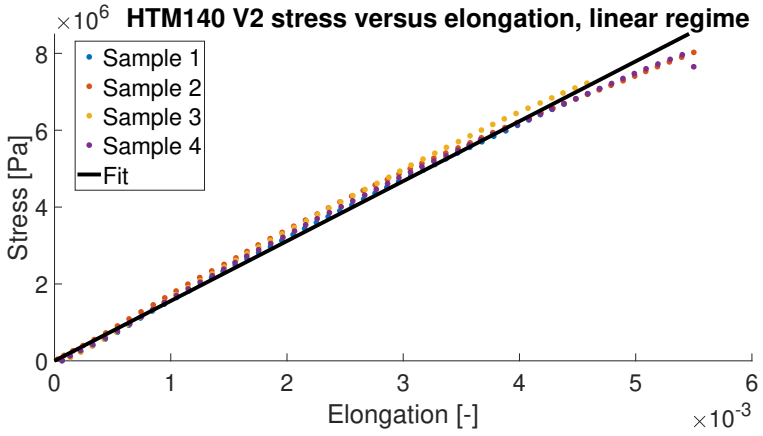

Figure 10: The linear regime of the tensile loading with added fit used to calculate the tensile modulus

Similarly, the Young's modulus of the 3DM Tough Clear material was obtained with a smaller test strip. For this material, the dimensions of the ASTM D638 test strip dimensions were divided by 4. The tensile test resulted in a tensile modulus of 1.84 GPa for this material.

(b) MATLAB functions

After reading the time domain data, the maximum amplitude of the triggered pulse is found and saved. This maximum is used to take the 1000 samples before and 5000 samples after the peak to determine the power spectrum. Due to the short rise time, 1000 samples is more than enough, while 5000 samples give enough space for the pulse to settle. The amplitude of the pulse is then normalised. Finally, the signal is zero-padded with 4000 zeros. We use a linear polynomial on the envelope of the time and logarithmic pulse amplitude for the settling time determination. Subsequently, the absolute of the inverse of this fit was taken as the settling time, similar to Dutta et al. [13]. During this paper, we used three important MATLAB functions to obtain the mode frequencies from the experimental data. These were: `pwelch`,`tfestimate` and `findpeaks`. Each of these functions will be shortly explained in this section.

(i) `pwelch` and `tfestimate`

In MATLAB, `pwelch` can be used to estimate the Welch's power spectral density. Using the Welch method, we reduce the effect of noise in our estimate by averaging over multiple repetitions of the signal. We use the time domain input of the axial or radial side for this function. Furthermore, to reduce spectral leakage, we used a Hanning window with a window size of 2500 samples. We chose this value after inspecting multiple windowing options. An overlap of 50 % of the window size prevents data loss from windowing. Finally, we inserted the sampling frequency for consistency between the methods.

We used the `tfestimate` function as a method of cross-checking the results. This function calculates the transfer function between time-domain input x and time-domain output y. The function converts these time-domain data to the frequency domain and divides the output by the input. In order to keep consistency between the cross-check and the method used to obtain the Welch's power spectrum, we used the same values for the Hanning window and overlap during conversion.